CHEMICAL AND THERMAL MODULATION OF MOLECULAR MOTOR ACTIVITIES

by

Weili Hong

A dissertation submitted to the faculty of
The University of Utah
in partial fulfillment of the requirements for the degree of

Doctor of Philosophy

in

Physics

Department of Physics and Astronomy

The University of Utah

August 2015

The University of Utah Graduate School

STATEMENT OF DISSERTATION APPROVAL

The dissertation of **Weili Hong**

has been approved by the following supervisory committee members:

Michael Vershinin	, Chair	**12/15/2014** Date Approved
Saveez Saffarian	, Member	**12/15/2014** Date Approved
Jordan Gerton	, Member	**12/15/2014** Date Approved
James Keener	, Member	**12/15/2014** Date Approved
Markus Babst	, Member	**12/15/2014** Date Approved

and by **Carleton DeTar** , Chair/Dean of

the Department/College/School of **Physics and Astronomy**

and by David B. Kieda, Dean of The Graduate School.

ABSTRACT

Molecular motors of kinesin and dynein families are responsible for various intracellular activities, from long distance movement of organelles, vesicles, protein complexes, and mRNAs to powering mitotic processes. They can take nanometer steps using chemical energy from the hydrolysis of ATP (adenosine triphosphate), and their dysfunction is involved in many neurodegenerative diseases that require long distance transport of cargos. Here I report on the study of the properties of molecular motors at a single-molecule level using optical trappings.

I first studied the inhibition properties of kinesin motors by marine natural compound adociasulfates. I showed that adociasulfates compete with microtubules for binding to kinesins and thus inhibit kinesins' activity. Although adociasulfates are a strong inhibitor for all kinesin members, they show a much higher inhibition effect for conventional kinesins than for mitotic kinesins. Thus adociasulfates can be used to specifically inhibit conventional kinesins. By comparing the inhibition of kinesins by two structurally similar adociasulfates, one can see that the negatively charged sulfate residue of adociasulfates can be replaced by other negative residues and thus make it possible for adociasulfate-derived compounds to be more cell permeable.

Kinesins and dyneins move cargos towards opposite directions along a microtubule. Cargos with both kinesins and dyneins attached often move bidirectionally due to undergoing a tug-of-war between the oppositely moving kinesin and dynein motors. Here

I studied the effect of temperature on microtubule-based kinesin and dynein motor transport. While kinesins' and dyneins' velocities are closely matched above 15 °C, below this temperature the dyneins' velocity decreases much faster than the kinesins'. The kinesins' and dyneins' forces do not measurably change with temperature. The results suggest that temperature has significant effects on bidirectional transport and can be used to probe tug-of-war mechanism between kinesins and dyneins.

TABLE OF CONTENTS

ACKNOWLEDGEMENTS

I would like to begin my acknowledgements by expressing my sincere gratitude to my advisor, Professor Michael Vershinin, for his constant support, mentoring, and guidance throughout my graduate study. I really appreciate his constant encouragement and trust for my research and the flexible and comfortable research environment he created.

I greatly appreciate the participation of my committee members, Professor Saveez Saffarian, Jordan Gerton, James Keener, and Markus Babst, for their time spend on my behalf.

I want to thank my current group members, Olaolu Osunbayo, Jared Bergman, and Leslie Mershon, for their great help during my research and for their beneficial discussions, and my former group member Jacqualine Butterfield.

I want to thank all my collaborators: Thomas Smith and Prof. Chris Ireland, for the adociasulfates they provided; Caitlin Lazar, Sarah Weil, and Prof. Richard Valle, for the dynein they provided; and Anjneya Takshak and Prof. Ambarish Kunwar for their simulation.

I would like to specially thank my family, for their understanding and unconditional support for my studies. I would also like to thank my friends, for their company and the pleasant time spent during this period.

CHAPTER 1

EXPERIMENTAL SETUP AND OPTICAL TRAPPING

INTRODUCTION

1.1 Experimental Setup

We constructed a high resolution microscope (built around Nikon eclipse Ti-U) with two optical trapping capabilities (Figure 1.1), conventional trapping and holographic trapping (Figure 1.2).[1] This microscope (Figure 1.3) can serve as a conventional compound light microscope: the light from the illumination source (Nikon Intenslight C-HGFI) is focused on the sample stage through a microscope condenser (**MC**) and is collected by the microscope objective (**MO**); the images are captured by any of several available video cameras. By adding one polarizing filter and one Normaski-modified Wollaston prism each before the **MC** and after the **MO** to the light path, an operator can turn this microscope into a **DIC** (differential interference contrast) microscope. By sending the light from the illumination source to the **MO** instead of the **MC** and adding excitation and emission filters to the light path, an operator can turn this microscope into an epi- or **TIRF** (total internal reflection fluorescence) microscope.

1.1.1 Conventional Trap Setup

For the conventional trapping setup, the setup has a 0.6 watt, 980 nm single mode fiber laser, and a commercially available fiberport is used to collimate the laser beam. The laser

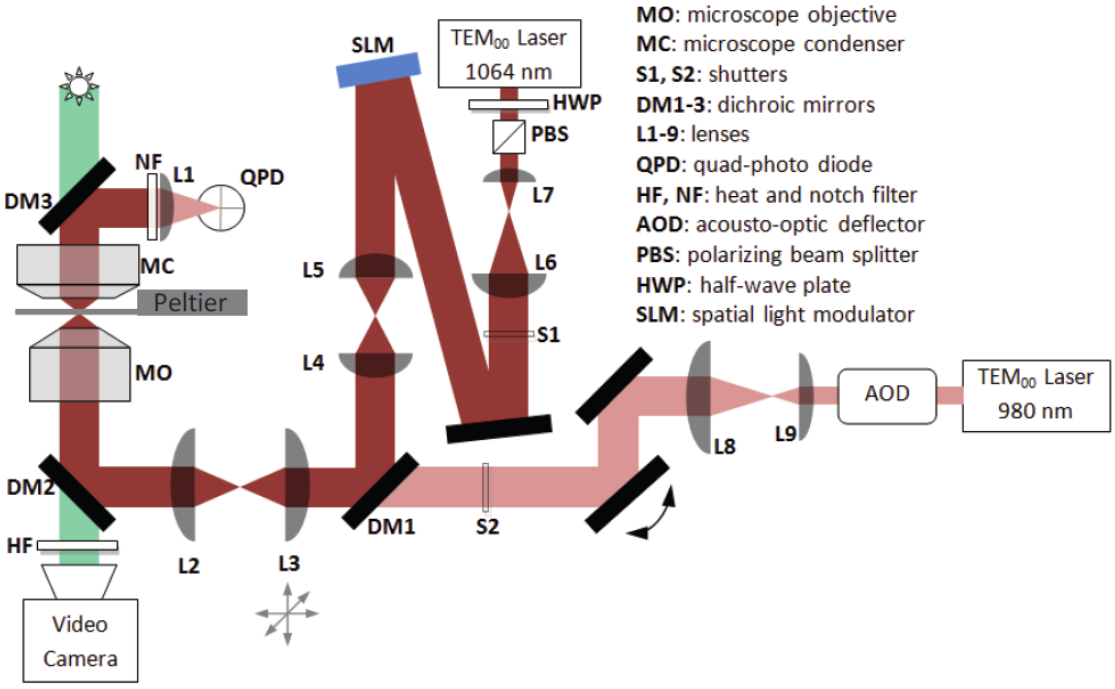

Figure 1.1 Schematic figure of experimental setup with optical trappings.

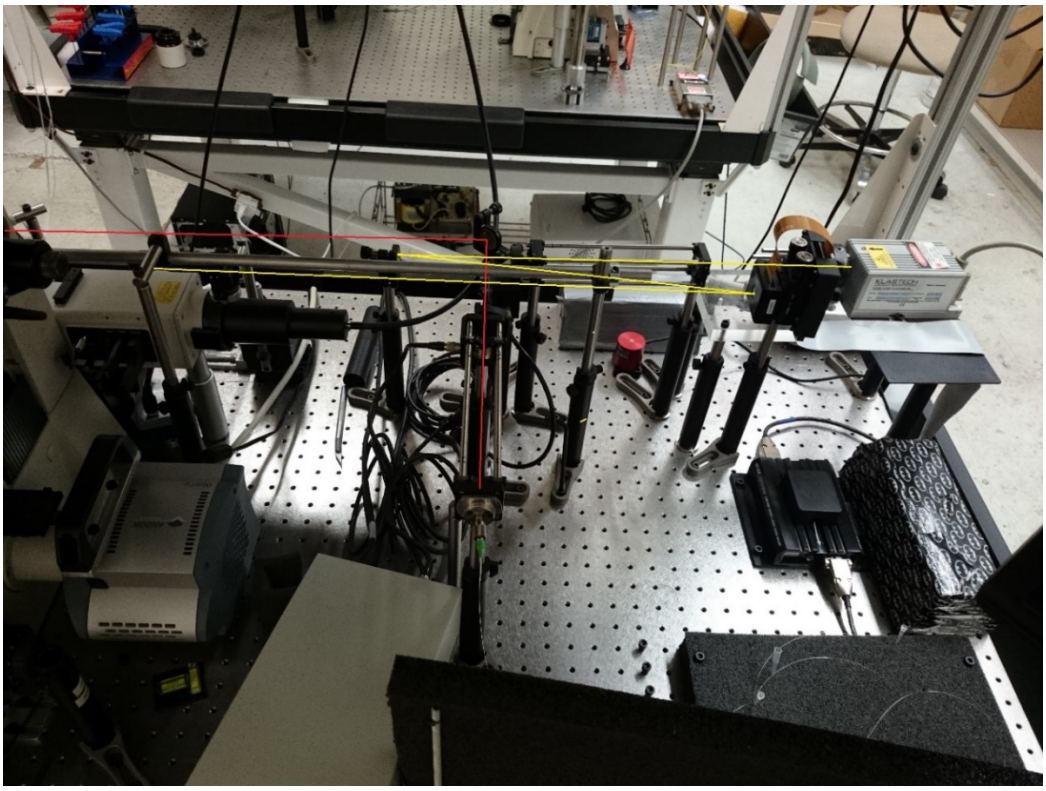

Figure 1.2 Optical trappings alignment. Red line shows the path of the 980 nm laser; yellow line shows the path of 1064 nm laser.

beam is then guided to pass a beam expander, which consists of lens 8 and lens 9 (labeled as **L8** and **L9**). The beam can be optionally steered using either acousto-optic deflectors (AODs) or a high speed computer-controlled mirror. Lenses 2 and 3 **(L2** and **L3**) allow for manual beam steering. The beam is then focused on the specimen stage by microscope objective (**MO**) to generate optical trapping. The outgoing laser beam is collected by microscope condenser (**MC**) and projected on the quadrant photodiode (**QPD**) by a dichroic mirror.

1.1.2 Holographic Trap Setup

For the holographic trapping setup, the setup has a 1 watt, 1064 nm solid state laser, and the laser beam is vertically polarized and guided through a half-wave plate (**HWP)**

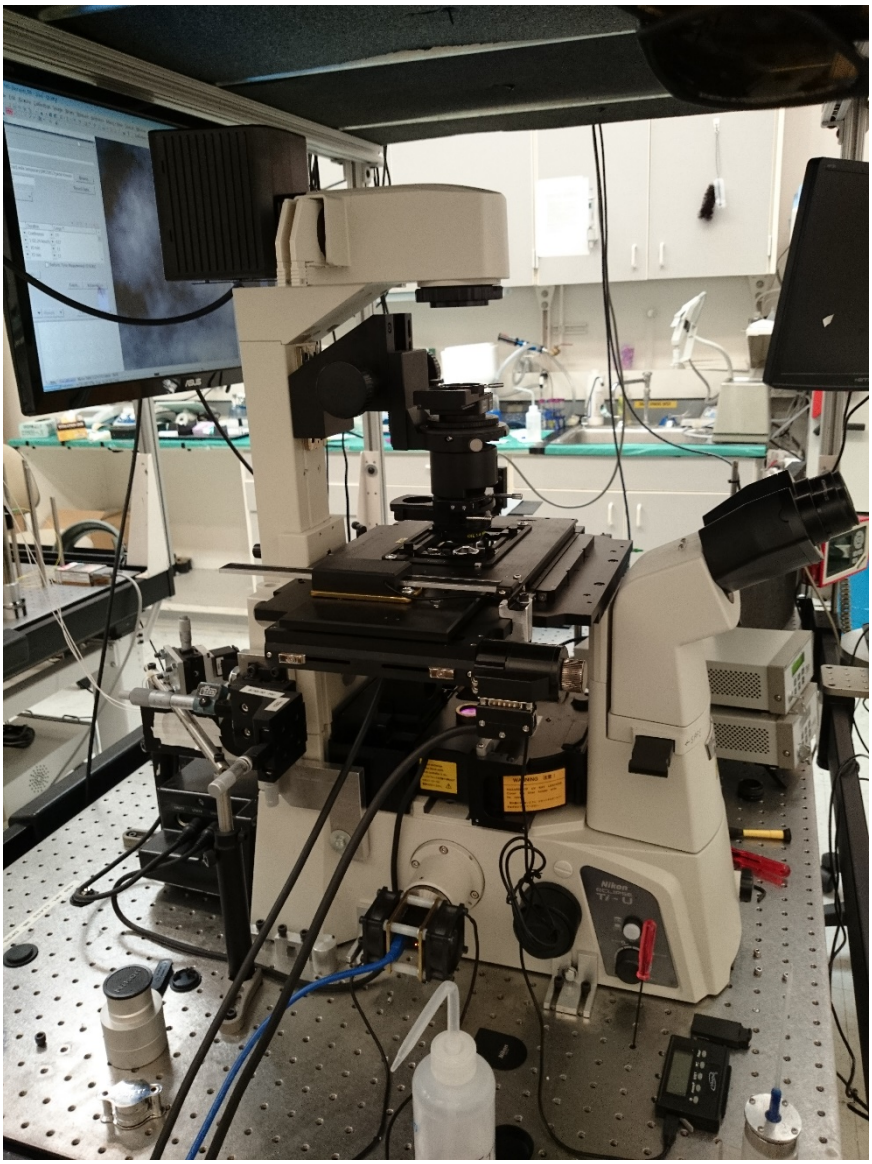

Figure 1.3 Microscope stage.

and a polarizing beam splitter (**PBS)** to produce vertically polarized laser beam of known power (often reduced below 1W). After the beam power is set, it is then expanded (lenses **L7** and **L6)** and then hits the spatial light modulator (**SLM**) at a very shallow angle. The **SLM** is located in a plane conjugate to the back-focal plane of the microscope objective. The beam diameter is closely matched to the size of the **SLM** active surface, although this is imperfect because the beam cross-section is circular while the mirror is rectangular. The laser beam is then reduced (lenses **L4** and **L5**), and the unrefracted part of the laser beam is optionally filtered out by a beam blocker. The beam is then merged to the conventional trapping path by a dichroic mirror (**DM1**), which reflects the 1064 nm laser and passes the 980 nm laser. Both 980 nm and 1064 nm beams enter the objective with beam diameter slightly overfilling the back-focal plane aperture.

1.2 Optical Trapping Details

1.2.1 Beam Expander

A beam expander usually consists of two positive focal length lenses, one with a large focal length and one with a small focal length, **L8** and **L9** in Figure 1.1 for example. For convenience, the focal lengths of all lenses (**L1** to **L9**) are defined as $f1$ to $f9$. The lens with small focal length **L9** is on the incoming beam side, and the lens with large focal length **L8** is on the outgoing beam side; the distance between these two lenses is set to be the sum of the focal lengths $f9 + f8$ so that after the beam expander, the beam width is expanded by $\frac{f8}{f9}$ times.

The purpose of getting a larger beam width is to fill or slightly overfill the back aperture of the microscope objective (**MO**).[2] Since the trapping ability depends on the gradient of the beam at the focused point, a more tightly converged laser beam will achieve a better

trap.

1.2.2 Beam Steering

A beam steering consists of two positive focal length lenses, with the same focal lengths, lenses **L2** and **L3** in Figure 1.1 for example. The distance between them is the sum of their focal lengths $f2 + f3$. Lens **L3** can be adjusted in all three dimensions and needs to be located at a place conjugated to the microscope objective back-focal plane. To do so, the distance between lens **L2** and the back-focal plane of the objective needs to be $2 \times f2$. Approximately, movement of the lens **L3**, corresponds to the movement of the laser trap in the sample plane. Thus, beam steering allows for convenient adjustment of the trap and thus is especially useful during trap alignment.

1.3 Principles of Optical Trapping

The full theory of how optical trapping works is quite complicated, and even fifth order perturbation theory calculations do not always precisely agree with measurements. However, for a few limiting cases, it can be explained easily. When the size of a particle d is much larger than the laser wavelength λ, $d \gg \lambda$, optical trapping theory can be explained using ray-optics. Figure 1.4 shows the principles of optical trapping.

The momentum of a light beam is proportional to its intensity and is in the direction of propagation. When the light beam passes through a dielectric sphere, refraction changes the direction of the light beam, which results in a momentum change between the incoming and outgoing light beams. According to the conservation of momentum law, the sphere experiences an equal and opposite momentum change, which is perpendicular to the light path inside the sphere and points to the outside of the sphere. Since momentum change

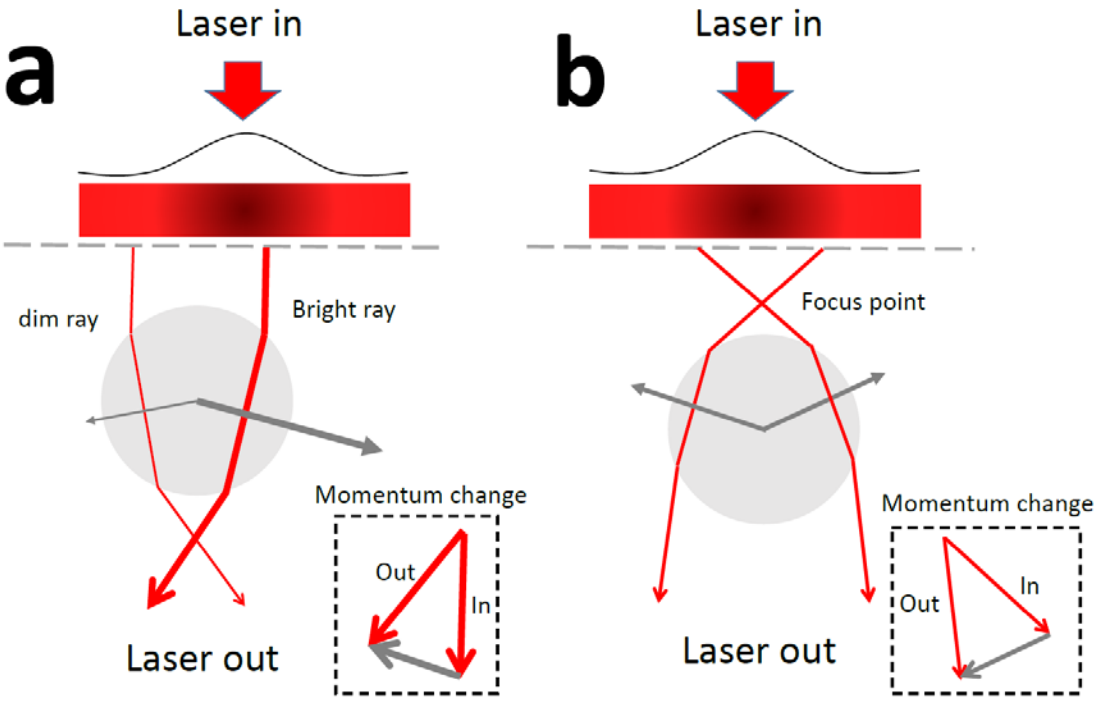

Figure 1.4 Ray-optics explanation of optical trapping. a: the dielectric sphere is side away from the trap center. The bright ray which is near the center and has a high intensity generates a larger momentum change than the dim ray which is near the margin and has low intensity. b: the sphere is away from the trap center in the light propagation direction, and the sum of the momentum changes on the sphere points to the trap center. Modified from reference [2].

over time is force, the sphere feels a force.

When a laser is focused at the sample plane, its intensity is Gaussian distributed (Figure 1.4), which means it has higher intensity in the center than the margins.

If a refractive sphere is not at the focal point of the laser beam, then we can figure out the direction of the net force as follows. Consider two rays going through the sphere symmetrically about its center. One ray is nearer to the beam center and the other nearer to the margin (Figure 1.4 a). Each of them generates a force on the sphere; however, the ray from the center will generate a larger force due to its higher intensity, so the sum of the forces for the two rays would be restoring towards the beam focus. However, some incident light will also reflect from the bead surface or scatter and absorb within the sphere. This results in a scattering force along the z direction. The scattering force tends to push the sphere out of the trap.

When the sphere is away from the trapping center in the z direction (Figure 1.4 b), the refracted ray will generate a force pointing to the trapping center, so the trap is in all three dimensions. To minimize the contribution of scattering force in the z direction, the laser beam needs to be focused as tightly as possible. We therefore used a high numerical aperture objective in our trapping experiment.

Let us consider a different limit. When the size of a particle d is much smaller than the laser wavelength λ, $d \ll \lambda$, the light cannot be represented by rays. However, full wave theory is not needed. A very small particle will be in a basically constant field and so can be viewed as a dipole. So the trapping can be viewed as a simple dipole-dipole interaction.

Unfortunately, most objects that we used for trapping have the size close to the laser wavelength, $d \sim \lambda$. For example, the laser wavelengths in our lab are 980 nm and 1064 nm,

and the beads sizes we used for trapping are 0.2 to 4 μm in diameter. The exact theory of optical trapping would be complicated; however, the trapping works well for particles in this region, and the force production can be easily calibrated.

1.4 Trap Stiffness Calibration

The restoring force F applied to a trapped bead, for bead displacement up to ~150 nm from the trapping center, is proportional to the displacement[4]

$$F = kx \tag{1.1}$$

Here k is the trap stiffness, which is the "spring constant" for the trapping, and x is the bead displacement from the trap center. Once the trap stiffness is known, the restoring force can be calculated from observed bead displacement.

The methods of calibrating trap stiffness have two categories: calibration of beads displacement against a known force (e.g., viscous drag force) or analysis of the thermal fluctuations of beads in a trap.[2] Here I discuss one calibration method as an example.

According to Stoke's law, the drag force F_v acting on a small sphere by viscous fluid is

$$F_v = 6\pi\mu R v \tag{1.2}$$

Here μ is the dynamic viscosity, R is the radius of the sphere, and v is the sphere's velocity.

After a bead is trapped, the flow cell that is fixed to a stepper motor stage in our setup (Bioprecision2, Ludle Electronic Products) is set to move at a constant velocity. When the bead stops to move relative to the trap center, the restoring force of the trap and the drag

force of the liquid are balanced. Then the trap stiffness can be calculated simply as $k = 6\pi\mu Rv/x$, where x is observed bead displacement from the trap center. This calibration must be performed at a known distance from the coveslip so that corrections for viscosity can be incorporated into the calibration.

1.5 Holographic Trapping

The key part of this holographic trapping system is the **SLM** (Figure 1.5), whose cross-section structure is shown in Figure 1.6. Our **SLM** has a display of size 7.68 nm $\times$ 7.68 nm, with 512×512 pixel electrodes in the bottom. Each pixel electrode can reflect light. Above pixel electrodes there is a transparent electrode and liquid crystals medium in between.

The orientations of liquid crystal particles in each cells can be modulated by an electric field. Another important property of liquid crystals is they are birefringent; i.e., they have different refractive indexes at different orientations. Thus by applying different electric fields within a cell, the refractive index of the medium in that cell can be modulated.

Back to the **SLM**, the laser light beam is incident on the face of **SLM**. It passes through the transparent electrode and liquid crystals medium and is reflected back by the reflective pixel electrodes. Voltage can be applied on each pixel electrode individually and the transparent electrode. The resulting electric field between pixel electrode and transparent electrode modulates the optical properties of liquid crystals, and thus the laser beam phase can be locally modulated. Thus interference patterns in space can be set by the phase pattern at the mirror. In practice, this process can be inverted. The **SLM** is connected to a computer and can be controlled by software. The operator can determine a light pattern that is desired, and the corresponding phase pattern is then calculated and set from the computer.

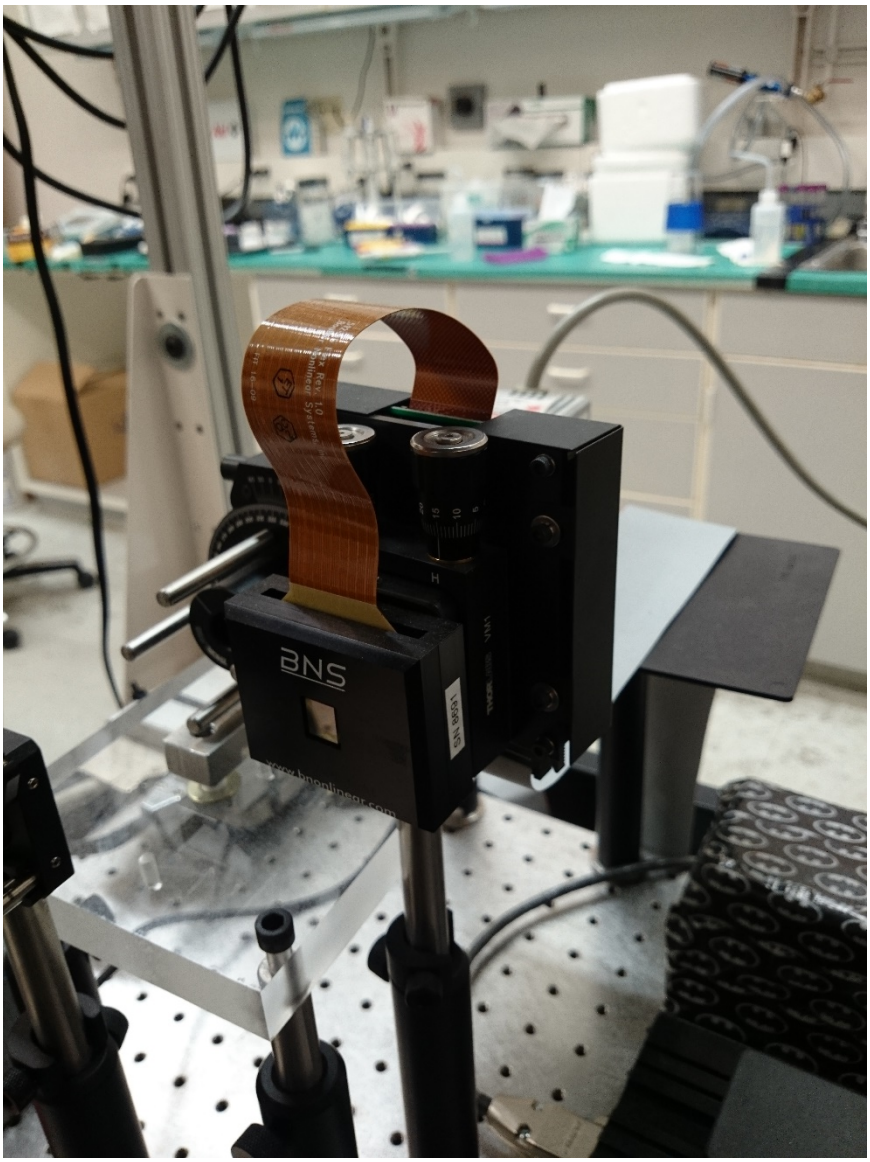

Figure 1.5 Spatial light modulator (SLM).

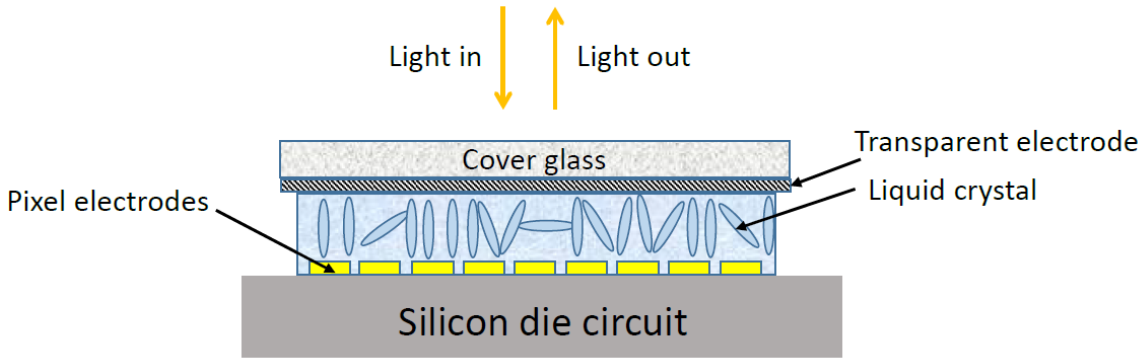

Figure 1.6 Spatial light modulator (SLM) cross section. Adapted from the manual.[3]

1.6 References

(1). Butterfield, J.; Hong, W.; Mershon, L.; Vershinin, M. Construction of a High Resolution Microscope with Conventional and Holographic Optical Trapping Capabilities. *J. Vis. Exp.* **2013**, Apr 22; (74).

(2). Svoboda, K.; Block, S. Biological Applications of Optical Forces. *Annu. Rev. Biophys. Biomol. Struct.* **1994**, *23*, 247–285.

(3). BNS Spatial Light Modulators XY Series from laser 2000 Manual. http://www.meadowlark.com/store/data_sheet/Datasheet_XYseries_SLM.pdf (accessed Oct 15, 2014).

(4). Svoboda, K.; Block, S. Force and Velocity Measured for Single Kinesin Motors. *Cell.* **1994**, *77*, 737–784.

CHAPTER 2

TEMPERATURE CALIBRATION

2.1 Introduction

Most of the experiments described in this thesis were via an *in vitro* approach using custom built flow chambers. To make a flow chamber, a coverglass and a coverslip are glued together by two strips of double sided tape (Scotch brand permanent double sided tape from 3M). The coverslips are usually pre-poly-lysinated (poly-L-lysine solution, 0.1% (w/v) in H_2O, from SIGMA) so that MTs can be attached to the surface. To increase the temperature cooling efficiency of the sample, I have replaced the coverglass used in a traditional flow chambers with a sapphire glass (model SP-114, from SwissJewel Company), which has much higher thermal conductivity (46 $W/(m \cdot K)$ for sapphire and ~1 $W/(m \cdot K)$ for glass). Despite the high up-front cost, the sapphire pieces can be reused. After each use, the flow chambers are immersed in acetone overnight, then the sapphire pieces can be easily removed from the coverslips and can then be cleaned with just liquid detergent and water.

A Peltier thermoelectric stage (Linkam PE 120) is used to control the sample temperature. In their design, during the cooling, the hot side of the Peltier device is cooled via pump driven water exchanger (if necessary), and the cold side sets the temperature of a copper plate. The plate has a hole that allows transmitted light from the microscopy to pass through, and the flow chambers can be mounted to the plate using clamps. The stage

was modified to fit an inverted microscope and eliminated most of the sample mounting material to minimize thermal mass (Figure 2.1). The flow chambers I used are small enough to securely attach to the copper plate with minimal custom made spring clips. The nominal stage temperature can be set from -25 °C to 120 °C with 0.1 °C precision. However, the actual sample temperature needs to be calibrated due to the sample exposure to the environment.

Precise temperature calibration is important for the experiments. Due to the small dimension of the flow chamber, it is hard to directly measure the temperature of the sample using thermometer, so I calibrated the temperature by adapting noncontact methods that have been recently reported in the literature.[2,3]

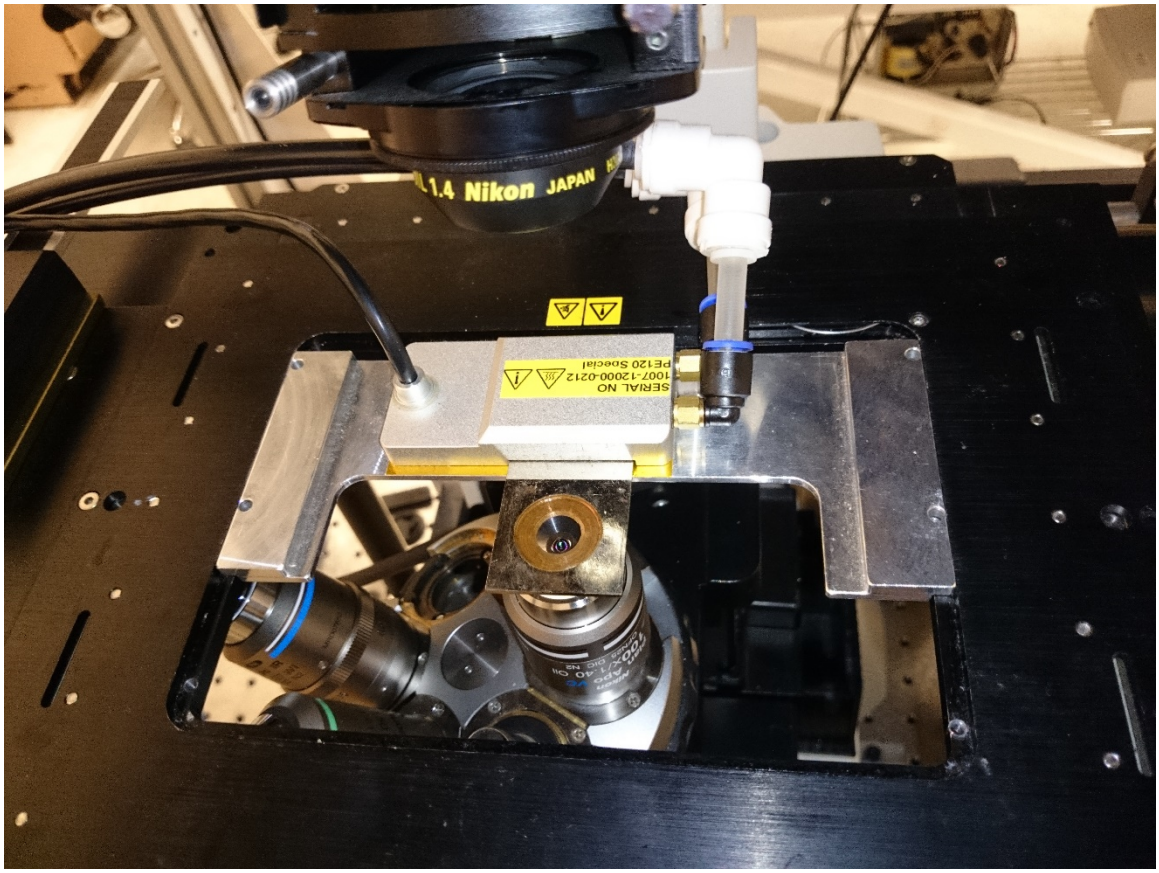

Figure 2.1 Linkam PE 120 Peltier thermoelectric stage after modification.

2.2 Temperature Calibration Using Quantum Dots

First, I calibrated the temperature using the thermal shift of quantum dots (QDs) fluorescence.[2,3]

The fluorescence of QDs are strongly temperature-dependent; the peak wavelength shifts linearly toward longer wavelengths as the temperature increases.[2,4] Therefore the temperature change can be estimated through the QDs peak wavelength shifts. The advantage of this method is that it is a noncontact measurement, and only the fluorescent spectrum needs to be collected.

First, I measured the spectrum shift of QDs (relative to room temperature baseline) as a function of temperature in a bench spectrophotometer where the solution temperature is known or can be easily measured, and used this as a reference. The actual sample temperature in our flow chambers could then be calibrated by recording the spectrum shift from room temperature of the same QDs in our flow chambers at different nominal stage temperatures.

I used CdSe QDs that were bought (from American Elements). CdSe QDs powder was diluted by 40% Ethylene Glycol in purified water; here Ethylene Glycol acts as a cryoprotectant.

2.2.1 Temperature Reference

For reference measurements, the spectra of QDs were measured using a Hitachi F-7000 spectrophotometer, with a temperature controller (TC 125 from Quantum Northwest) capable of controlling temperature from -55 °C to 105 °C. 70 µl micro UV-cuvette (from BRAND) was used to minimize the usage of QDs, and 200 µl QDs solution was added to overfill the cuvette. The actual temperature in the solution was calibrated by immersing K-

type thermocouples in the solution to measure the temperature directly. A digital thermometer (Nicety DT 804) was used for readout. I found the waiting time of ~15 minutes was sufficient for the solution temperature to become stable after each temperature change. For the temperatures set by the controller, -15 °C, -10 °C, 0 °C, 10 °C, 20 °C, 30 °C, and 60 °C, the solution temperatures were -10.5 °C, -7 °C, 2 °C, 10.5 °C, 20 °C, 29.5 °C, and 54.8 °C, respectively. Figure 2.2 shows the plot of solution temperature change with the set controller temperature. The solution temperature changes linearly with the controller temperature (relative to room temperature baseline).

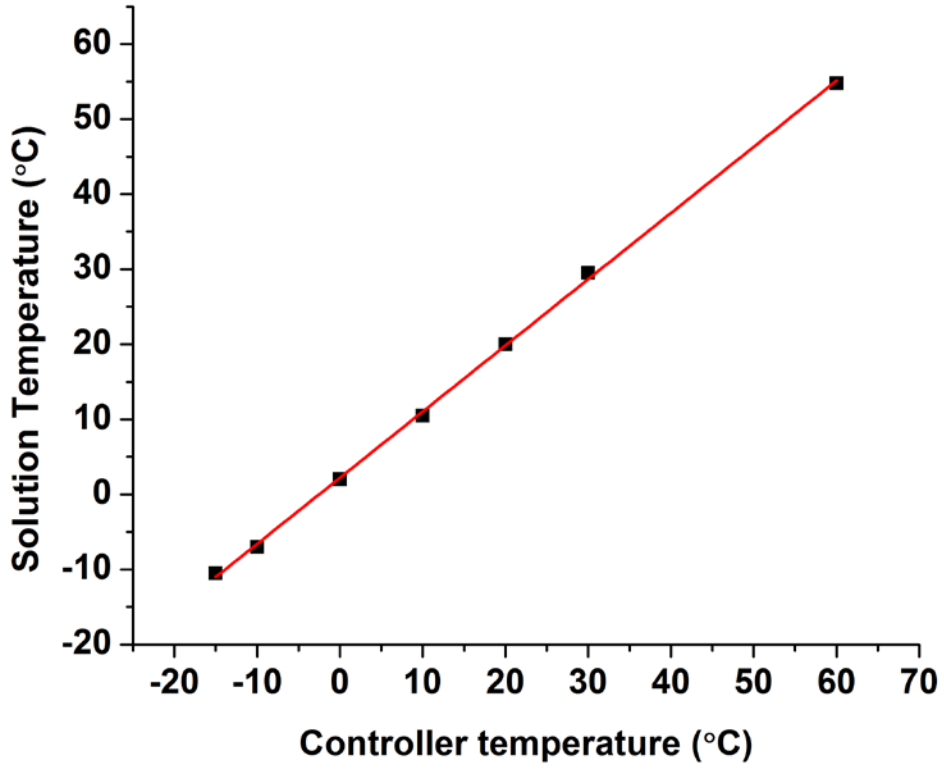

Figure 2.2 Hitachi F-7000 spectrophotometer stage. Solution temperature is linear with the controller temperature. The fitted slope is 0.880 ± 0.011.

Figure 2.3 shows the spectra of CdSe QDs at different temperatures. QDs solution was excited by 388 nm wavelength light, and each spectrum was acquired from 488 nm to 550 nm (scan speed 60 nm/mins), with 1 nm resolution. The spectrum peak was around 515 nm; as the temperature increases, the peak shifts to higher wavelengths. To get the peak wavelength, each spectrum was fitted to an exponential modified Gaussian distribution (Origin software, from Oringinlab) from 500 nm to 530 nm in wavelength (Figure 2.4). The fitted parameters were used to recalcultate the curve in Matlab and use these parameters to extract the precise peak value and position.

Figure 2.5 shows the peak wavelength changes as a function of temperature. The data

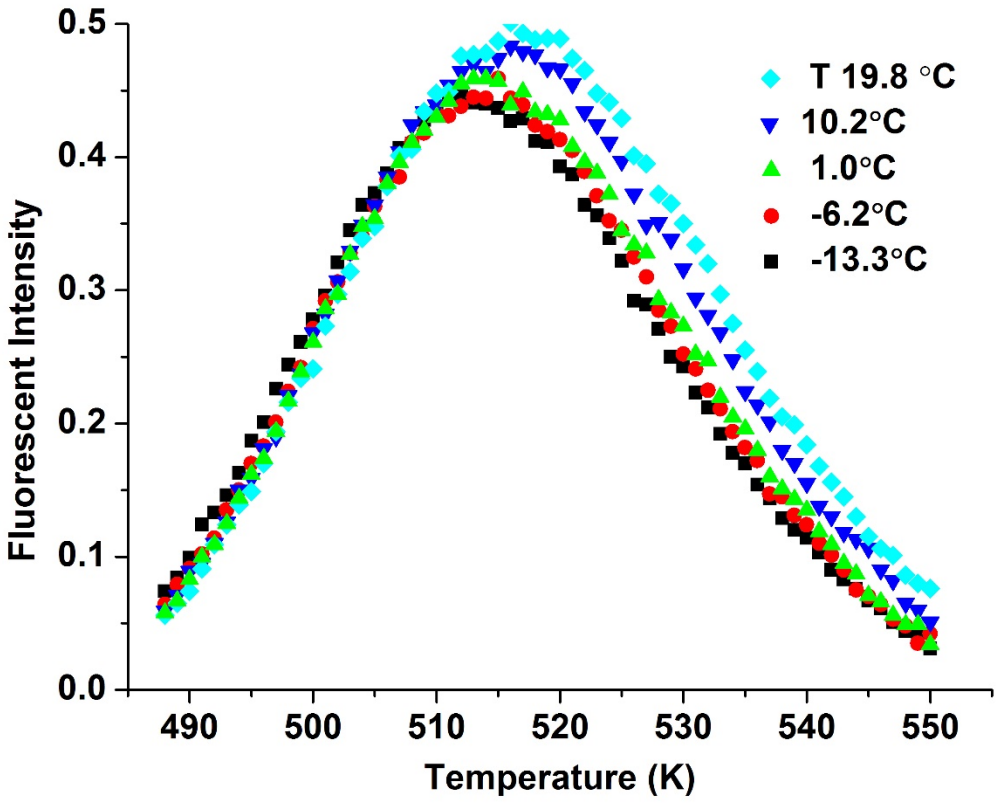

Figure 2.3 Spectra of CdSe QDs at different temperatures.

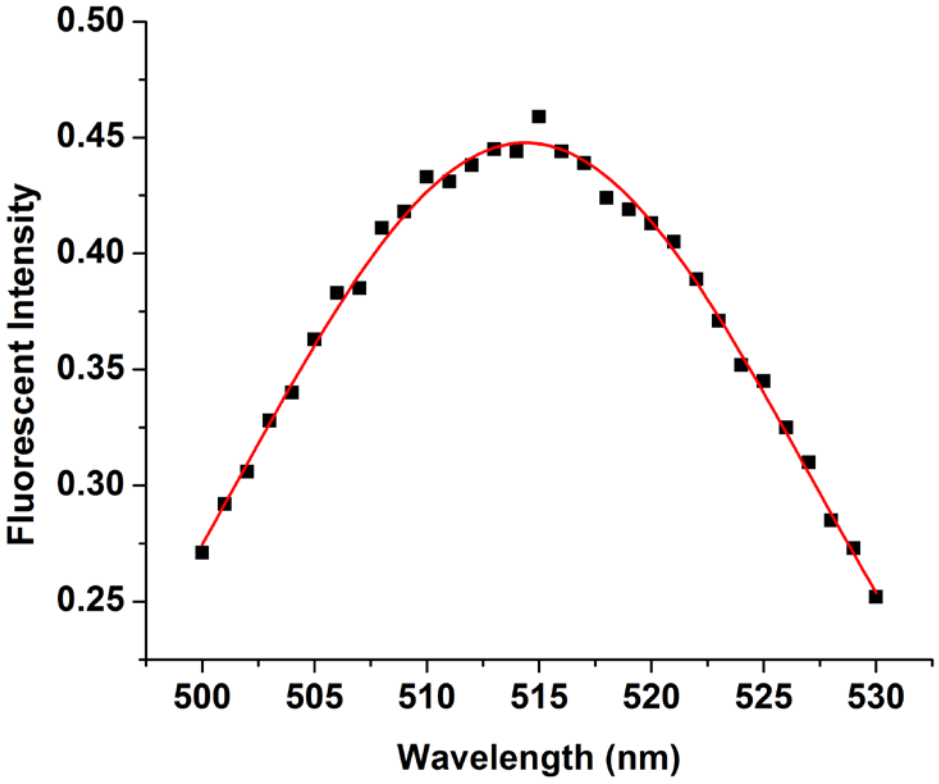

Figure 2.4 Modified Gaussian fit to the spectrum of QDs from 500–530 nm.

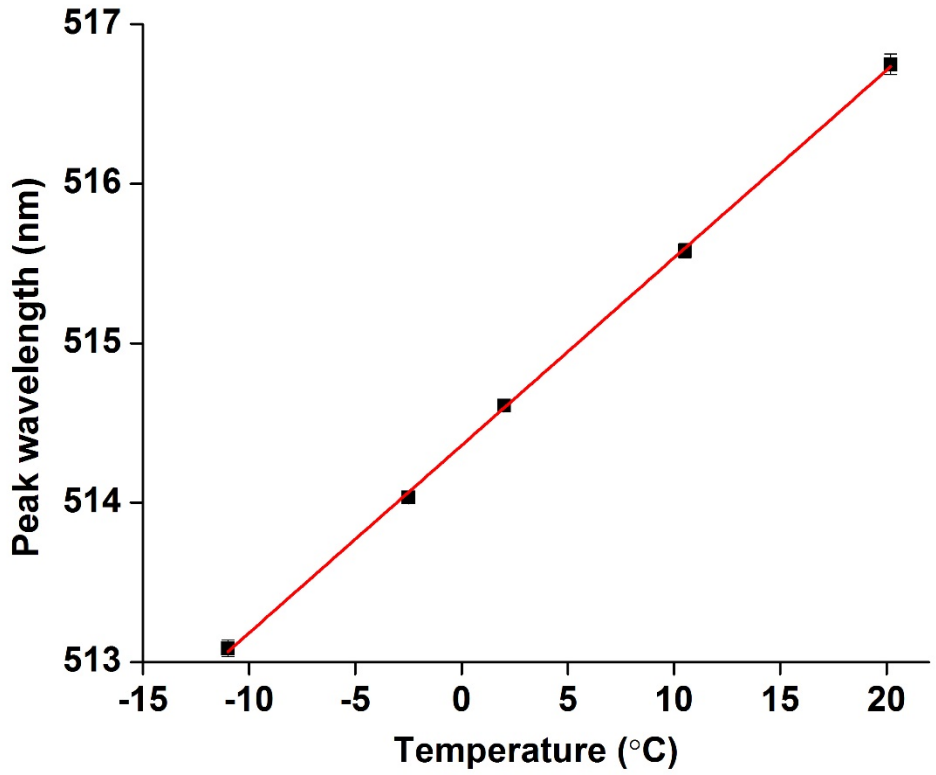

Figure 2.5 Peak wavelength of the CdSe QDs spectrum at different temperature. The fit is linear and the slope is 0.118 ± 0.001 nm/°C.

from -10.5 °C to 29.5 °C can be fitted to a linear line. The temperature range from -10.5 °C to 20 °C is roughly the range where most of the experiments were done. The peak wavelength shifts ~0.118 ± 0.001 nm/°C, consistent with previous results, which gave 0.105 nm/°C and 0.093 nm/°C.[4,5]

2.2.2 Temperature Measurement

Then I measured the spectrum shift of QDs in the flow chamber. A Peltier temperature controller (Linkam PE 120) is fixed on the microscope stage. The sapphire side of the flow chamber was attached to the copper plate of the temperature controller for maximized

thermal exchange and temperature stability. The excitation light has a wavelength of 408 nm by using a filter for the light lamp. A Nikon oil objective (100× with numerical aperture 1.40) was used to acquire the fluorescence of QDs. A spectrometer (SpectraPro 2300i from Princeton Instruments) was used to acquire the spectrum of QDs.

The spectrum of QDs acquired for temperature measurement was also fitted to a modified Gaussian distribution from 500-530 nm (Figure 2.6).

Figure 2.7 shows the measured CdSe QDs peak wavelength shifts as a function of temperature. The fitted slope is ~0.116 ± 0.003 nm/°C, close to the slope from the reference ~0.118 ± 0.001 nm/°C. This temperature is the nominal stage temperature set by the Peltier controller. Table 2.1 shows the measured sample temperature. Figure 2.8 shows the measured sample temperature changes with the set stage temperature.

Although the formula for temperature calibration looks precise, the error bars on the calibration from the fit are non-negligible: less than ±0.3 °C in the temperature range are of interest to us. However, this calibrated temperature probably has larger error bars. Firstly, the spectrum of QDs measured using Hitachi F-7000 spectrophotometer has low resolution (1 nm), which may result in larger error bars of the peak wavelength calculation. Also the peak wavelength at the same fixed temperature for the two sets of measurement is slightly but consistently different, suggesting slight calibration differences between the spectrophotometers used in the two sets of measurements. With these potential systematic errors accounted for, the precision of our calibration can be conservatively estimated at ±0.5 °C.

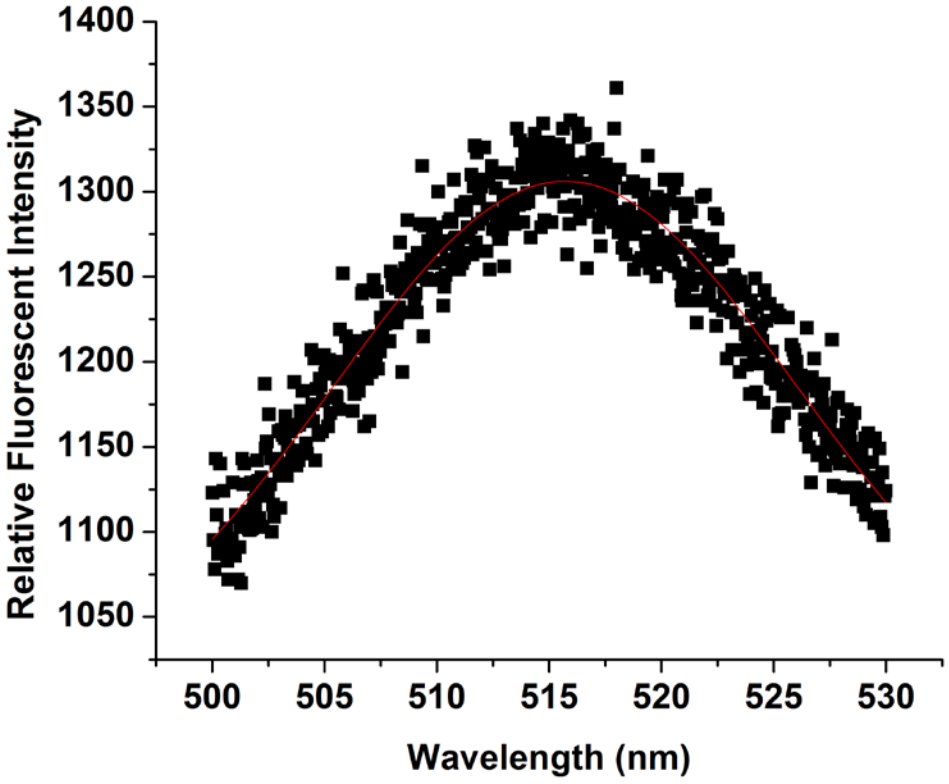

Figure 2.6 Microscope stage. Modified Gaussian fit of the spectrum of CdSe QDs at 0°C from 500–530 nm.

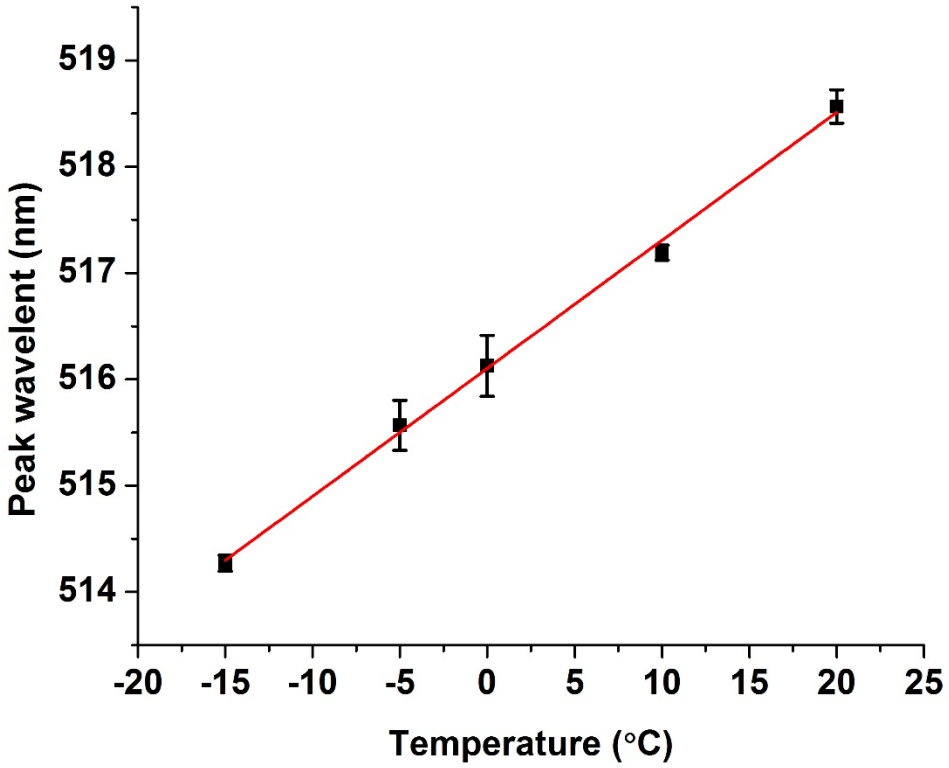

Figure 2.7 Peak wavelength shifts as a function of temperature. The fitted slope is 0.116 ± 0.003 nm/°C.

Table 2.1 Sample temperature calibration

Set stage temperature	Measured sample temperature
-10 °C	-9.5 ± 0.1 °C
0 °C	0.4 ± 0.1 °C
10 °C	10.2 ± 0.1 °C
20 °C	20.0 ± 0.2 °C
30 °C	29.9 ± 0.3 °C

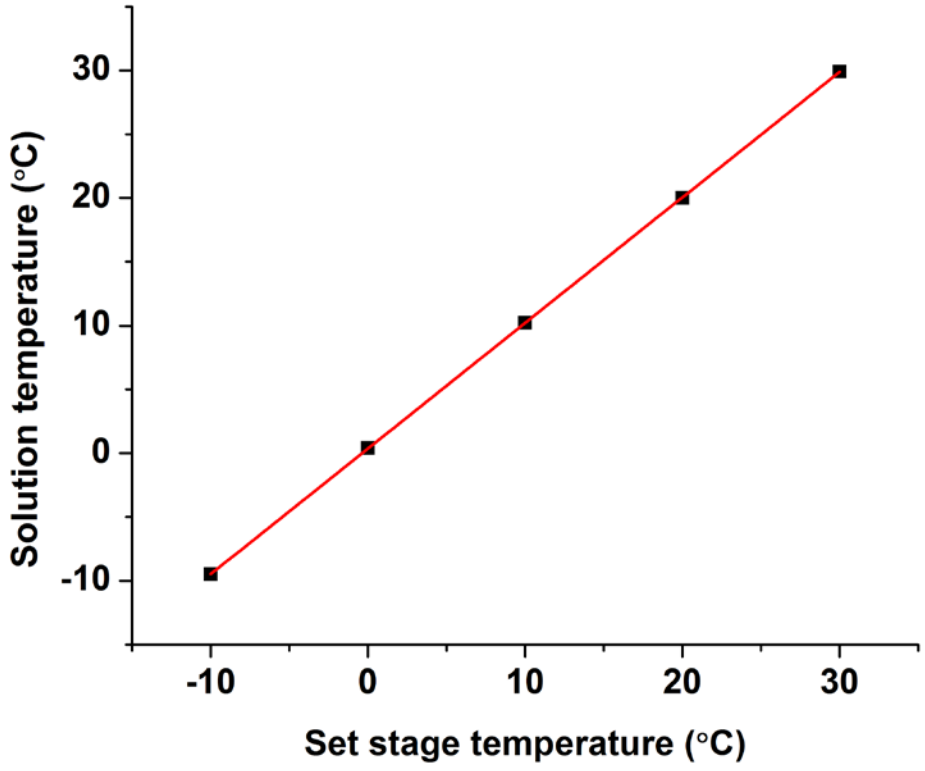

Figure 2.8 Measured sample temperature changes linearly with the set stage temperature. The fitted slope is 0.984 ± 0.001.

2.3 Temperature Calibration Using Beads Diffusion

The temperature-dependent effect of the diffusion coefficient is described by Walden's rule

$$\frac{D_1\eta_1}{T_1} = \frac{D_2\eta_2}{T_2} \tag{2.1}$$

Here D is the diffusion coefficient, η is the solvent viscosity, and T is the absolute temperature.[6] The accuracy of this rule was extensively tested with macromolecules over a temperature range from 1–37 °C, and the deviation was within 4%.[7] Polystyrene latex beads (0.038 μm in diameter) were also tested over the temperature range 0–50 °C, and no significant deviation was found.[6]

I used this rule to calibrate the temperature in flow chamber. Polystyrene beads (0.5 μm in diameter) were diluted in deionized water with low concentration. At this concentration, only one bead can be found in the field of view (~20 μm × 20 μm) to make sure the bead-bead interaction can be negligible. The bead was trapped by optical trapping, brought 3 μm above the surface. At this height, the viscosity applied on the bead is 1.05 times the viscosity of the water.[8] The trapping was then turned off and the images were recorded by an Andor camera. The diffusion coefficient can be gotten from the track of the bead trace over time.

This experiment was done over stage temperature from -10 °C to 30 °C. The solution temperature calibrated was close to the previous results. However, the systematic errors proved higher, and therefore QDs calibration is preferred.

2.4 Temperature Calibration using Measurements of Freezing Point

I also tried to calibrate the solution temperature in the flow chamber by measuring the freezing point of a few substances, including purified water ddH_2O, heavy water D_2O (from United Nuclear), ethylene glycol (from MICRON Chemicals) water mixture, and dimethyl sulfoxide (DMSO, from VWR).

For purified water ddH_2O, the freezing point is 0 °C. For heavy water D_2O, the freezing point is 3.8 °C.[9] The freezing point of DMSO is 18.5 °C.[10]

To avoid the supercooling effect, I measured the freezing point by freezing the substance and then measured at which temperature it started to melt. The substance states can be directly observed on the live view from the camera.

For example, for ddH_2O, which has a freezing point of 0 °C, I first set the stage temperature at -8 °C to freeze it completely, then increased the stage temperature to -2 °C, close to but still below the freezing point. If melting was not observed for 10 minutes, then I increased the temperature by 0.5 °C, waited for another 10 minutes, and so on until melting was observed.

Table 2.2 shows the substances measured, the stage temperature when the substance started to unfreeze, and the freezing point. I used the freezing point temperature as the calibrated solution temperature at this stage temperature. Figure 2.9 shows the calibrated solution temperature changes with the stage temperature.

When I used oil objective for the temperature calibration, oil was added between the objective and the flow chamber, the calibrated solution temperature is higher than that using air objective. For solution temperature ~0 °C when air objective was used, the

Table 2.2 Freezing point measurement

Substance	Freezing point (°C)	Set stage temperature (°C)
ddH_2O	0	-1
Heavy water D_2O	3.8	3
Dimethyl Sulfoxide (DMSO)	18.5	18

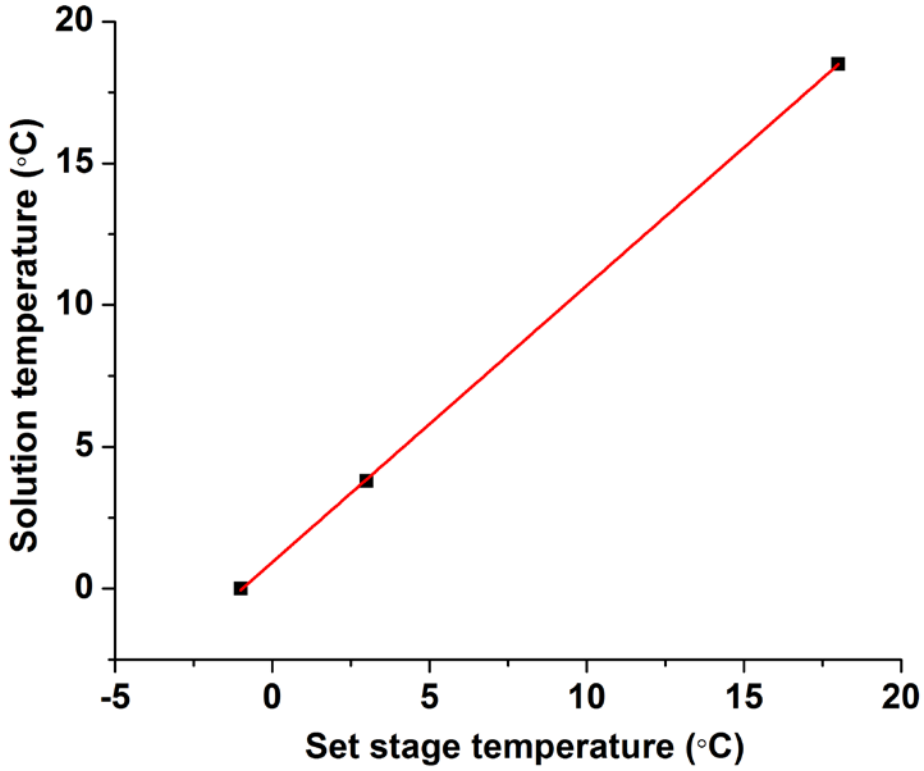

Figure 2.9 Calibration by measuring freezing point. Calibrated temperature changes linearly with the stage temperature. The fitted slope is 0.975 ± 0.005.

solution temperature was ~1 °C when oil objective was used. The solution temperature when oil objective was used was adjusted accordingly.

2.5 References

(1). Butterfield, J.; Hong, W.; Mershon, L.; Vershinin, M. Construction of a High Resolution Microscope with Conventional and Holographic Optical Trapping Capabilities. *J. Vis. Exp.* **2013**, Apr 22 (74).

(2). Maestro, L. M.; Jacinto, C.; Silva, U. R.; Vetrone, F.; Capobianco, J. A.; Jaque, D.; Solé, J. G. CdTe Quantum Dots as Nanothermometers: Towards Highly Sensitive Thermal Imaging. *Small* **2011**, *7* (13), 1774–1778.

(3). Yang, J. M.; Yang, H.; Lin, L. Quantum Dot Nano Thermometers Reveal Heterogeneous Local Thermogenesis in Living Cells. *ACS Nano* **2011**, *5* (6) 5067–5071.

(4). Li, S.; Zhang, K.; Yang, J. M.; Lin, L. W.; Yang, H. Single Quantum Dots as Local Temperature Markers. *Nano Lett.* **2007**, *7* (10), 3102–3105.

(5). Joshi, A.; Narsingi, K. Y.; Manasreh, M. O.; Davis, E. A.; Weaver, B. D. *Appl. Phys. Lett.* **2006**, *89* 131907.

(6). Fernandez, A; and Phillies, G. Temperature Dependence of the Diffusion Coefficient of Polystyrene Latex Spheres. *Biopolymers* **1983**, *22* (2), 593–595.

(7). Longsworth, L. G. *J. Phys. Chem.* **1954**, *58*, 770–773.

(8). Svobada, K.; Block, S. Biological Applications of Optical Forces. *Annu. Rev. Biophys. Biomol. Struct.* **1994**, *23*, 247–285.

(9). Wikipedia. Heavy Water. http://en.wikipedia.org/wiki/Heavy_water#cite_note-7 (accessed Oct 15, 2014).

(10). VWR. Dimethyl Sulfoxide, ACS Grade. https://us.vwr.com/store/catalog/product.jsp?product_id=4541152 (accessed Oct 15, 2014).

CHAPTER 3

MOLECULAR MOTORS

3.1 Introduction

Cytoskeletal molecular motors are responsible for intracellular transport of many kinds of cargoes.[1] They use the chemical energy from triphosphate hydrolysis to drive conformational changes that generate motile force.[1] There are three large superfamilies of cytoskeletal molecular motors: kinesins, dyneins, and myosins. They perform a wide variety of tasks in cells, of which I want to highlight one. Kinesins and dyneins are MT-based molecular motors that are responsible for long range movement across the whole cell, and myosins are actin-based molecular motors that are responsible for shorter range movement, often nearer to cell periphery.[1] Kinesins usually move toward the plus end of MTs, and dyneins usually move toward the minus end of MTs, though notable exceptions like the kinesin-14 family motors have been reported and thoroughly studied. The molecular motors I studied are the conventional kinesin KIF5A, a member of the kinesin-1 family; Eg5 and BimC, both members of kinesin-5 family, which is mostly involved in mitosis; and cytoplasmic mammalian dynein.

3.2 Microtubules

Microtubules (MTs) are one of the three kinds of cytoskeleton filaments in cells. They provide mechanical support for cell shapes and act as tracks for MT-based molecular

motors to move cargoes.[2] MTs are hollow tubes that are formed by α- and β-tubulin heterodimers (Figure 3.1). Alternating α- and β-tubulins form linear substructures called protofilaments (Figure 3.2), which are locally oriented parallel to the tube axis. They are then stacked laterally to cover the surface of the tube while leaving the center hollow (Figure 3.3). Tubulins in neighboring protofilaments shift a little bit with respect to each other in the axial direction, forming a left-handed helical order.[3] This structure ensures that one end of the MTs always have α-tubulin exposed, which is defined as the (-) end, and the other end would always have β-tubulin exposed, which is defined as the (+) end.

The distance between the neighboring α- or β-tubulins is ~8 nm, which is the typical step size for kinesin and dynein; the outside diameter of MTs is ~ 25 nm.

3.3 Kinesin Introduction

Kinesin superfamily motors have 14 recognized families, based on the results of phylogenetic analysis.[4] Based on the general roles, kinesins can be grouped into kinesins responsible for general transport, kinesins for mitosis, and unusual kinesins (e.g., chromokinesins, and kinesin-13 MT stability factors). Most kinesin members move toward the plus end of MTs; however, there are some kinesins (kinesin-14 family motors) that

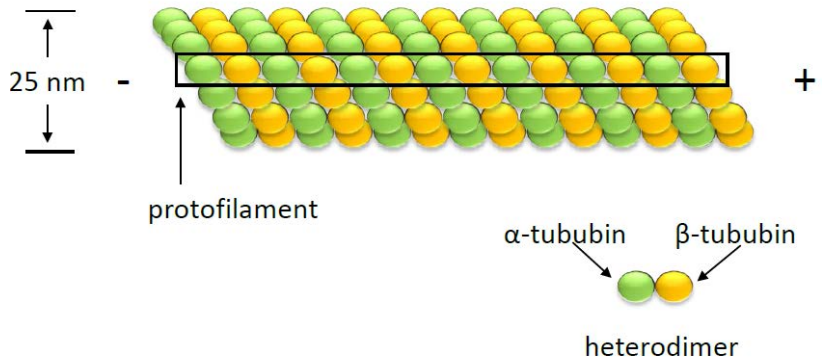

Figure 3.1 Helical structure of microtubule. Modified from reference [25].

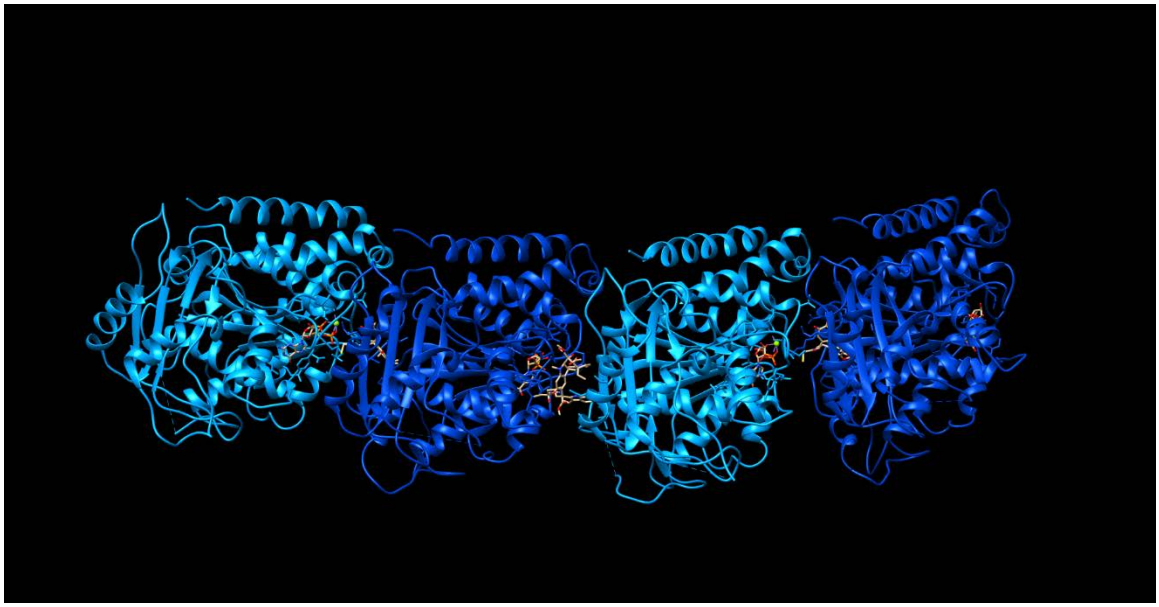

Figure 3.2 A protofilament-like structure formed by alternating α- and β tubulins. Adapted from structure of 1Z2B from PDB (protein data bank).[22] Reprinted with permission from RCSB PDB.

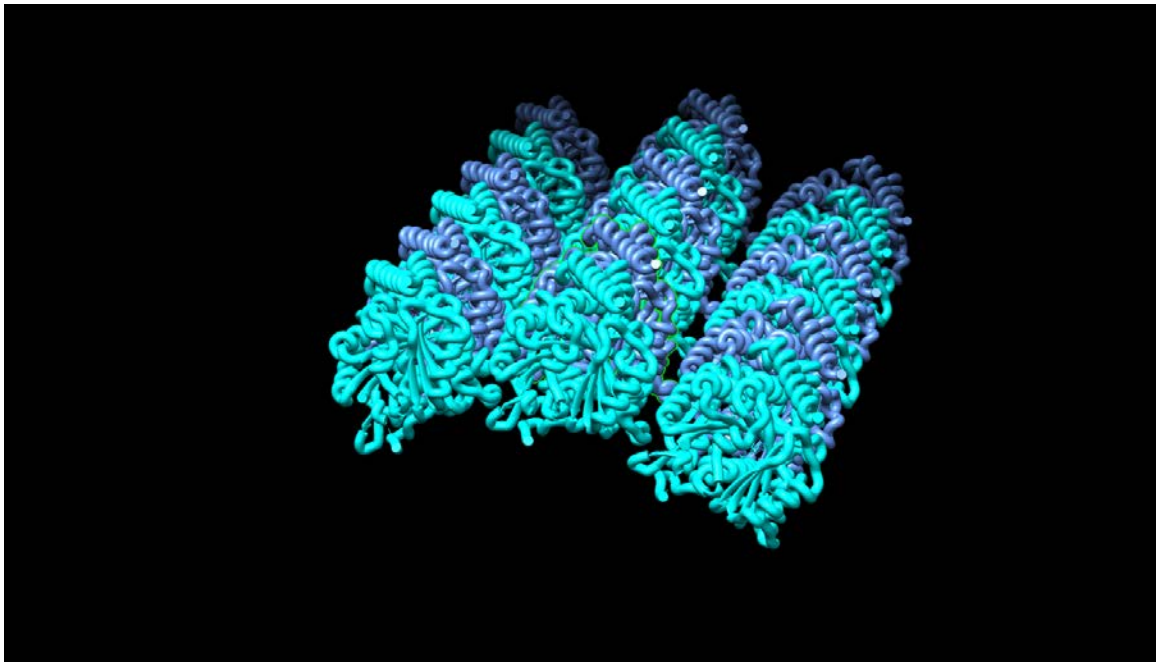

Figure 3.3 Profilaments stacking into a tube. Adapted from structure of 3J6F from PDB.[23] Reprinted with permission from RCSB PDB.

move toward the minus end of MTs.

3.3.1 Kinesin Structure

Conventional kinesin (kinesin-1) is the first discovered and most studied in the kinesin family. Kinesin-1 motors are homodimers that consist of two heavy chains (HCs) and two light chains (LCs) (Figure 3.4).[5]

At the N-terminus of HCs there are motor domains (also termed as “heads”). Each head can bind to MTs and hydrolyze ATP. The two heads in a dimer are connected by short strings of residues (also termed as the “neck linkers”). The neck linkers are further connected to a long dimerization region (also termed as the “stalk”). The dimerization domain is composed of coiled-coil segments interrupted by less ordered regions that act as hinges. This gives kinesin significant lateral and rotational flexibility.

At the C-terminus of HCs there is the cargo binding domain, a region responsible for kinesin self-inhibition and LCs binding regions. The LCs also play a role in kinesin self-

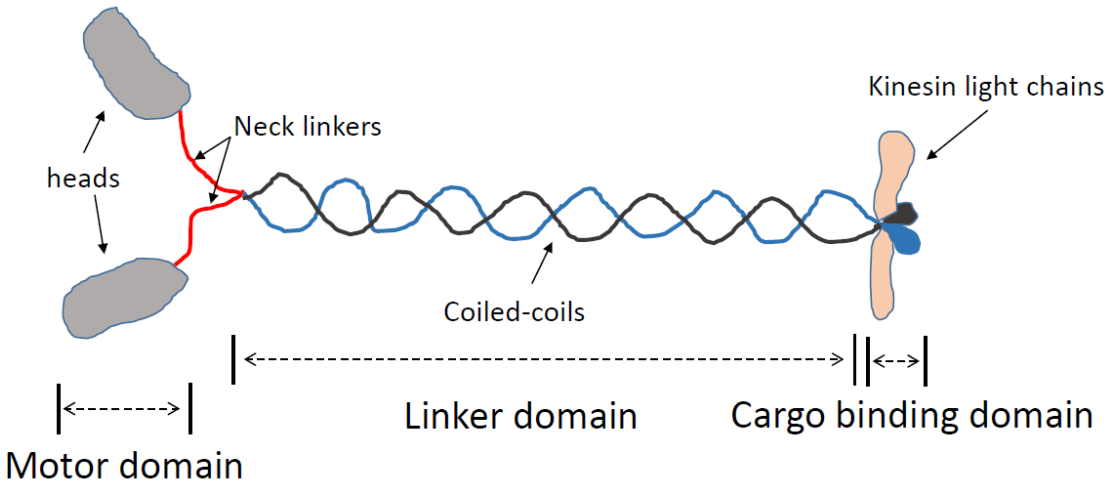

Figure 3.4 Structure of kinesin-1. Modified from reference [5].

inhibtion and cargo binding. For our *in vitro* studies, where kinesin is not self-inhibited and cargo binding is done either nonspecifically or through a tag, the LCs may be dispensable. However, it is best to work with full length KIF5A recombinant HCs if one aims to preserve the motor flexibility and stability that is often lost in shorter recombinant HCs.

The neck linker, a string of ~ 12 amino-acids that is highly conserved in plus-end but not minus-end kinesin motors, plays an important role in the processive movement of kinesin.[6] For MT bound kinesin head without a nucleotide, ATP binding generates a conformational change in the neck linker (a "powerstroke"), docking the neck linker onto the head in the MT plus end direction.[6] Since ATP preferentially binds to the forward head, the neck linker docking biases the backward head toward the plus end direction.

3.3.2 Kinesin Stepping

Conventional kinesin is a highly processive motor. It can take more than 100 consecutive steps without detachment from MTs, and the center-of-mass step size is 8 nm,[7,8] the adjacent tubulin dimer displacement. While stepping, kinesin hydrolyzes one ATP per step.[10] Kinesin walks in a "hand-over-hand" pattern,[9,10] meaning one head passes the other one alternatively, with each trailing head taking 16 nm step and becoming the new leading head, alternatively.[10]

3.3.3 Kinesin Binding to Microtubules

Kinesin binds to MTs through many interactions,[13] with a strong electrostatic component. The primarily positively charged residues of kinesin heads interact with the primarily negatively charged residues of tubulins.[13] Figure 3.5 shows the structure of one kinesin motor domain binding to α/β tubulin dimer of MT derived from cryo-electron

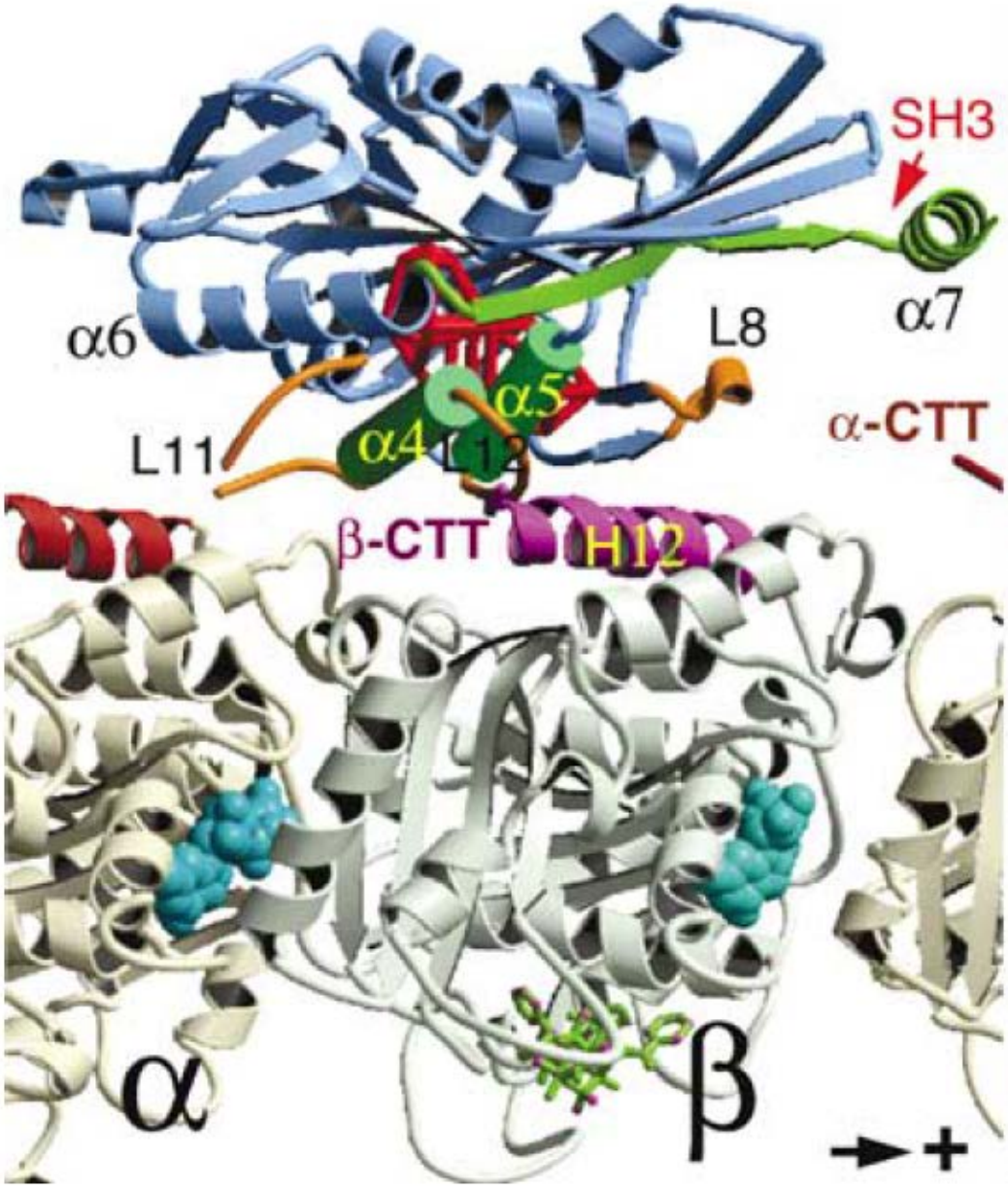

Figure 3.5 Structure of kinesin motor domain binding to MT. Adapted from reference [12]. Reprinted with permission from John Wiley and Sons.

microscope images. The structure of kinesin head can be divided into three parts: seven β sheets lie in the middle; three α helices, α1, α2, and α3 on top; and three α helices, α4, α5, and α6 on the bottom. The bottom helices and several key loops (L8, L11, and L12) form the primary MT interaction side. The nucleotide binding site is located at the interface of all three parts of kinesin.

The cryo-electron microscope structure of kinesin-MT complex shows that the structural elements of L7, L8, L11, L12, α4, α5, and α6 from kinesin are close to helices H11, H12, the loop between H11-12, and the C-terminus end of both α- and β- tubulins.[11] Studies of point mutant proteins have shown that primarily positive charged residues, clustered in loops L7, L8, L11, L12, and helix α4, α5 from kinesin [13] and negative residues in helix H11, H12, and the loop connecting them from α- and β- tubulins [11] are responsible for kinesin-MTs binding.

3.4 Cytoplasmic Dynein Introduction

Dyneins, based on their functions, can be grouped into two classes: axonemal dyneins and cytoplasmic dyneins.[14,15] Axonemal dyneins are responsible for ciliary and flagellar movement; cytoplasmic dyneins are involved in a wide range of functions from cargoes transport in cells to mitosis.[14,15] Dyneins usually contain two or three heavy chain units (~350 kDa), which are the largest subunits of the full dynein complex and are responsible for ATP hydrolysis and MT-binding and a variety of accessory subunits: intermediate chains, light intermediate chains, and light chains.

3.4.1 Cytoplasmic Dynein Structure

Figure 3.6 is the cartoon view of cytoplasmic dynein. Cytoplasmic dynein is composed of two heavy chains (HC) and a few accessory chains. The two heavy chains dimerize at the N-terminus tail domain; two intermediate chains (IC) and two light intermediate chains (LIC) directly bind to the heavy chain, and three dimers of light chains (LC) bind to the intermediate chains (IC).[17] The motor domain is at the C-terminus of the heavy chain. Each heavy chain consists of a ring of six AAA+ (ATPase associated with various cellular activities) domains, labeled as AAA1-6. AAA1-4 can bind and hydrolyze ATP, with the

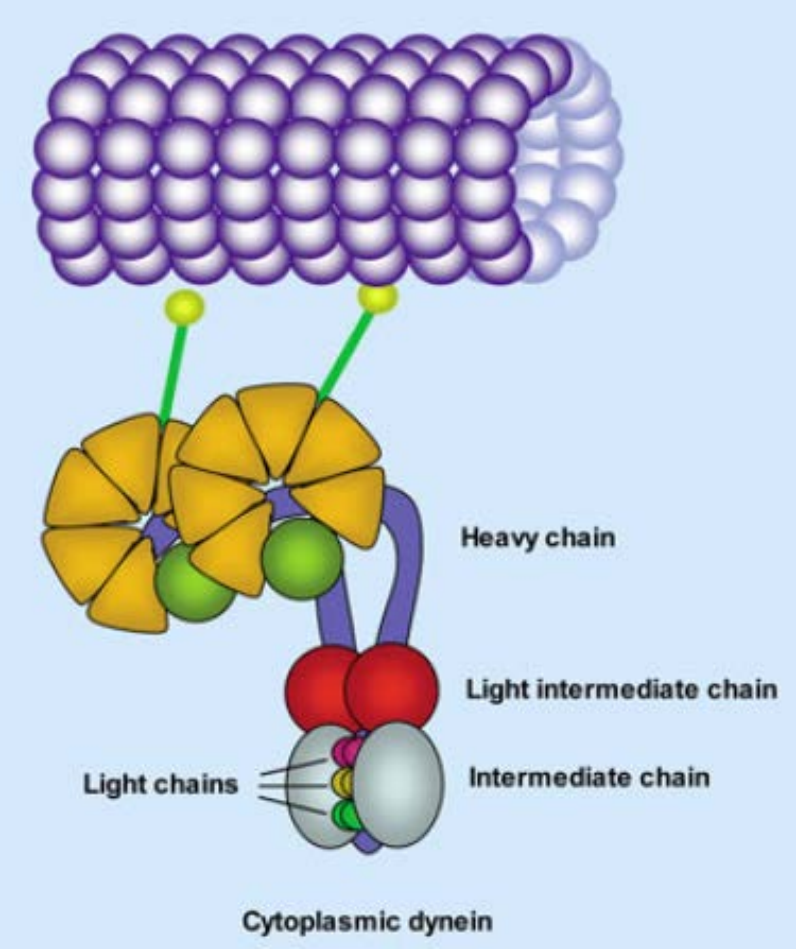

Figure 3.6 Cytoplasmic dynein composition and domain structure. Adapted from reference[19]. Reprinted with permission from the Journal of Cell Science.

ATP hydrolysis at AAA1 and AAA3 being particularly important for motility, and the ATP hydrolysis at AAA2 and AAA4 may only have a regulatory role.[16,18]

The linker domain, which starts from AAA1 and spans across the AAA+ rings, shifts its terminating position from AAA2 to AAA4 during the ATPase cycle.[20] This shifting is a significant part of the dynein powerstroke.[20]

The stalk is an extended structure (~15 nm long) formed by antiparallel coiled coils emerging from AAA4 and AAA5, respectively.[16] A globular structure formed at the end is the MT-binding domain. Recent studies showed that the shift of the registry of this coiled coil is responsible for allosteric communication between the head domain where the ATP is hydrolyzed and the MT-binding domain.[16]

3.4.2 Cytoplasmic Dynein Stepping

Cytoplasmic dynein is a processive motor, which can take ~1 μm movement before dissociation from MTs.[18] This is roughly the same length movement kinesin-1 can achieve; however, dynein step size is more variable. While dynein predominantly takes 8 nm center-of-mass steps, larger steps (as large as 32 nm) are also observed.[18] Dynein often take backward and sideway steps to the adjacent protofilament along MTs, which kinesin rarely does.[18] Studies showed that dynein stepping is highly variable and is not just hand-over-hand.[21,24]

3.5 References

[1]. Hirokawa, N.; Noda, Y.; Tanaka, Y.; Niwa, S. Kinesin Superfamily Motor Proteins and Intracellular Transport. *Nat. Rev. Mol. Cell Bio.* **2009**, *10*, 682–696.

[2]. Howard, J.; Hyman, A. A. Dynamics and Mechanics of the Microtubule Plus End *Nature* **2003**, *422*, 753–758.

[3]. Hunyadi, V.; Chretien, D.; Flyvbjerg, H.; Janosi, I. M. Why is the Microtubule Lattice Helical? *Biol. Cell* **2007**, *99*, 117–128.

[4]. Lawrence, C. J.; Dawe, R. K.; Christie, K. R.; Cleveland, D. W.; Dawson, S. C.; Endow, S. A.; Goldstein, L. S.; Goodson, H. V.; Hirokawa, N.; Howard, J.; Malmberg, R. L.; McIntosh, J. R.; Miki, H.; Mitchison, T. J.; Okada, Y.; Reddy, A. S.; Saxton, W. M.; Schliwa, M.; Scholey, J. M.; Vale, R. D.; Walczak, C. E.; Wordeman, L. A Standardized Kinesin Nomenclature. *J Cell Biol.* **2004**, *167* (1), 19–22.

[5]. Gennerich, A.; Vale, R. Walking the Walk: How Kinesin and Dynein Coordinate their Steps. *Curr. Opin. Cell Biol.* **2009**, 21, 59–67.

[6]. Rice, S. ; Lin, A.; Safer, D.; Hart, C.; Naberk, N.; Carragher, B.; Cain, S.; Pechatnikova, E.; Wilson-Kubalek, E.; Whittaker, M.; Pate, E.;Cookek, R.; Taylor, E.; Milligan, R.; Vale, R. A Structural Change in the Kinesin Motor Protein that Drives Motility. *Nature* **1999**, *402* (6763), 778–784.

[7]. Howard, J.; Hudspeth, A. J.; Vale, R. D. Movement of Microtubules by Single Kinesin Molecules. *Nature* **1989**, *342*, 154–158.

[8]. Svoboda, K.; Schmidt, C. F.; Schnapp, B. J.; Block, S. M. Direct Observation of Kinesin Stepping by Optical Trapping Interferometry. *Nature* **1993**, *365*, 721–727.

[9]. Asbury C.; Fehr A.; Block S. Kinesin Moves by an Asymmetric Hand-Over-Hand Mechanism. *Science* **2003**, *302* (5653), 2130–2134.

[10]. Yildiz, A.; Tomishige, M.; Vale, R.; Selvin, P. Kinesin Walks Hand-Over-Hand. *Science* **2004**, *303* (5658), 676–678.

[11]. Uchimura, S.; Oguchi, Y.; Hachikubo, Y.; Ishiwata, S.; Muto, E. Key Residues on Microtubule Responsible for Activation of Kinesin Atpase *EMBO J.* **2010**, *29* (7), 1167–1175.

[12]. Skiniotis, G.; Cochran, J. C.; Muller, J.; Mandelkow, E.; Gilbert, S. P.; Hoenger, A. Modulation of Kinesin Binding by the C-Termini of Tubulin. *EMBO J.* **2004**, *23*, 989–999.

[13]. Woehlke, G.; Ruby, A. K.; Hart, C. L.; Ly, B.; Hom-Booher, N.; Vale, R. D. Microtubule Interaction Site of the Kinesin Motor. *Cell* **1997**, *90* (2), 207–216.

[14]. Vallee, R. B.; Williams, J. C.; Varma, D.; Barnhart, L. E. Dynein: An Ancient Motor Protein Involved in Multiple Modes of Transport. *J. Neurobiol.* **2004**, *58*, 189–200.

[15]. Pfister, K.; Shah, P. R.; Hummerich, H.; Russ, A.; Cotton, J.; Annuar, A.; King, S.; Fisher, E. Genetic Analysis of the Cytoplasmic Dynein Subunit Families. *PLoS Genet.* **2006**, *2* (1), e1.

[16]. Carter, A. P.; Garbarino, J. E.; Wilson-Kubalek, E. M.; Shipley, W. E.; Cho, C.; Milligan, R. A.; Vale, R. D.; Gibbons, I. R. Structure and Functional Role of Dynein's Microtubule-Binding Domain. *Science* **2008**, *322* (5908), 1691–1695.

[17]. Vallee, R. B.; Wall, J. S.; Paschal, B. M.; Shpetner, H. S. Microtubule-associated Protein 1C from Brain is a Two-headed Cytosolic Dynein. *Nature* **1988**, *332*, 561–563.

[18]. Kardon, J.; Vale, R. Regulators of the Cytoplasmic Dynein Motor. *Nat. Rev. Mol. Cell Biol.* **2009**, *10*, 854–865.

[19]. Hook, P.; Vallee, R. B. The Dynein Family at a Glance. *J Cell Sci.* **2006**, *119* (21), 4369–4371.

[20]. Roberts, A. J.; Numata, N.; Walker, M. L.; Kato, Y. S.; Malkova, B.; Kon, T.; Ohkura, R.; Arisaka, F.; Knight, P. J.; Sutoh, K.; Burgess, S. A. AAA+ Ring and Linker Swing Mechanism in the Dynein Motor. *Cell* **2009**, *136* (3), 485–495.

[21]. Qiu, W.; Derr, N. D.; Goodman, B. S.; Villa, E.; Wu, D.; Shih, W.; Reck-Peterson, S. L. Dynein Achieves Processive Motion Using Both Stochastic and Coordinated Stepping. *Nat Struct. Mol. Biol.* **2012**, *19* (2), 193–200.

[22]. Image from the RCSB PDB (www.rcsb.org) of PDB ID 1Z2B (Gigant, B.; Wang, C.; Ravelli, R. B.; Roussi, F.; Steinmetz, M. O.; Curmi, P. A.; Sobel, A.; Knossow, M. Structural basis for the regulation of tubulin by vinblastine. *Nature* **2005**, *435*, 519–522).

[23]. Image from the RCSB PDB (www.rcsb.org) of PDB ID 3J6F (Alushin, G. M.; Lander, G. C.; Kellogg, E. H.; Zhang, R.; Baker, D.; Nogales, E. High-resolution microtubule structures reveal the structural transitions in αβ-tubulin upon GTP hydrolysis. *Cell* **2014**, *157*, 1117–1129).

[24]. DeWitt, M. A.; Chang, A. Y.; Combs, P. A.; Yildiz, A. Cytoplasmic Dynein Moves Through Uncoordinated Stepping of the AAA+ Ring Domains. *Science* **2012**, *335* (6065), 221–225.

[25]. Molecular Expressions, Cell biology and microscopy structure and function of cells & viruses, Microtubules. http://micro.magnet.fsu.edu/cells/microtubules/microtubules.html (accessed Oct 25, 2014).

CHAPTER 4

INHIBITION OF KINESIN BY ADOCIASULFATES

4.1 Adociasulfates Introduction

Kinesin usually moves cargos along MTs by consuming the energy from ATP hydrolysis. In the absence of MTs, kinesin hydrolyzes ATP very slowly. The basal ATPase rate is <0.01/s per kinesin head; upon binding to MTs, the MT-stimulated ATPase rate increases >1000 times.[3] Thus an otherwise active kinesin's ATPase activity would be greatly inhibited if it could not bind to MTs.

Adociasulfates (AS) are a group of small compounds that are isolated from marine sponges. They are a subfamily of sulfated triterpenoid hydroquinone.[1] They first received attention as a strong inhibitor for kinesin family motors,[3] and they inhibit kinesin activity by targeting kinesin motor domain and compete for MT binding, with little effect on nucleotide binding to kinesin,[3] and this inhibitory effect is linked to at least one sulfate group of adociasulfates.[2]

People were interested in AS because at the time they were the only natural products that were known to have inhibitory effect on kinesin-MT binding; however, there soon emerged some problems that limit their potential therapeutic applications.

First of all, the sulfate residue of AS is strongly negative, and the overall molecules are fairly large (~700g/mol). Such molecules generally have low permeability across lipid bilayers such as the cell membranes. Permeability of course varies by cell and organism

type but in general AS would be hard to get into the cells. So its utility as a research reagent and for drug development is limited.

Second of all, a recent study observed that AS tends to form rodlike aggregates in solution.[4] They suggested that instead of AS inhibiting kinesin individually, aggregated AS mimics the activity of MTs. The aggregated AS would potentially expose a line of negatively charged sulfates that could potentially mimic MT protofilaments that expose many negative residues on the surface. This was an appealing mechanism in which AS could conceivably compete with MTs for kinesin binding and inhibits kinesin's ATPase acitivity.[4] So even if AS could get into the cells, aggregation could also cause problems for cell functions.

Finally, although AS was shown to have specificity for kinesin family motors inhibition,[3] it was not clear whether AS was further specific to some kinesins more than others.

I addressed these issues individually.

4.1.1 Structure of Adociasulfates

Figure 4.1 shows the structures of some AS. The common structures are the steroid core and the benzylated ring with residues at the 2′ and 5′ positions. The sulfate residue is either at the 2′ position or at 5′ position, or at both.

Of these AS, AS-2 (**4**), AS-10 (**6**), and AS-6 (**7**) are strong inhibitors of kinesin, with the half inhibition concentration IC_{50} value to be 2–6 μM, and the full inhibition concentration to be 15 μM.[2,3,6] By directly comparing AS-2 and AS-6, their structure only differs at the 2′ position, where the sulfate residue is replaced by H^+, so the sulfate residue at this position does not contribute to the inhibition significantly. By comparing AS-2 and

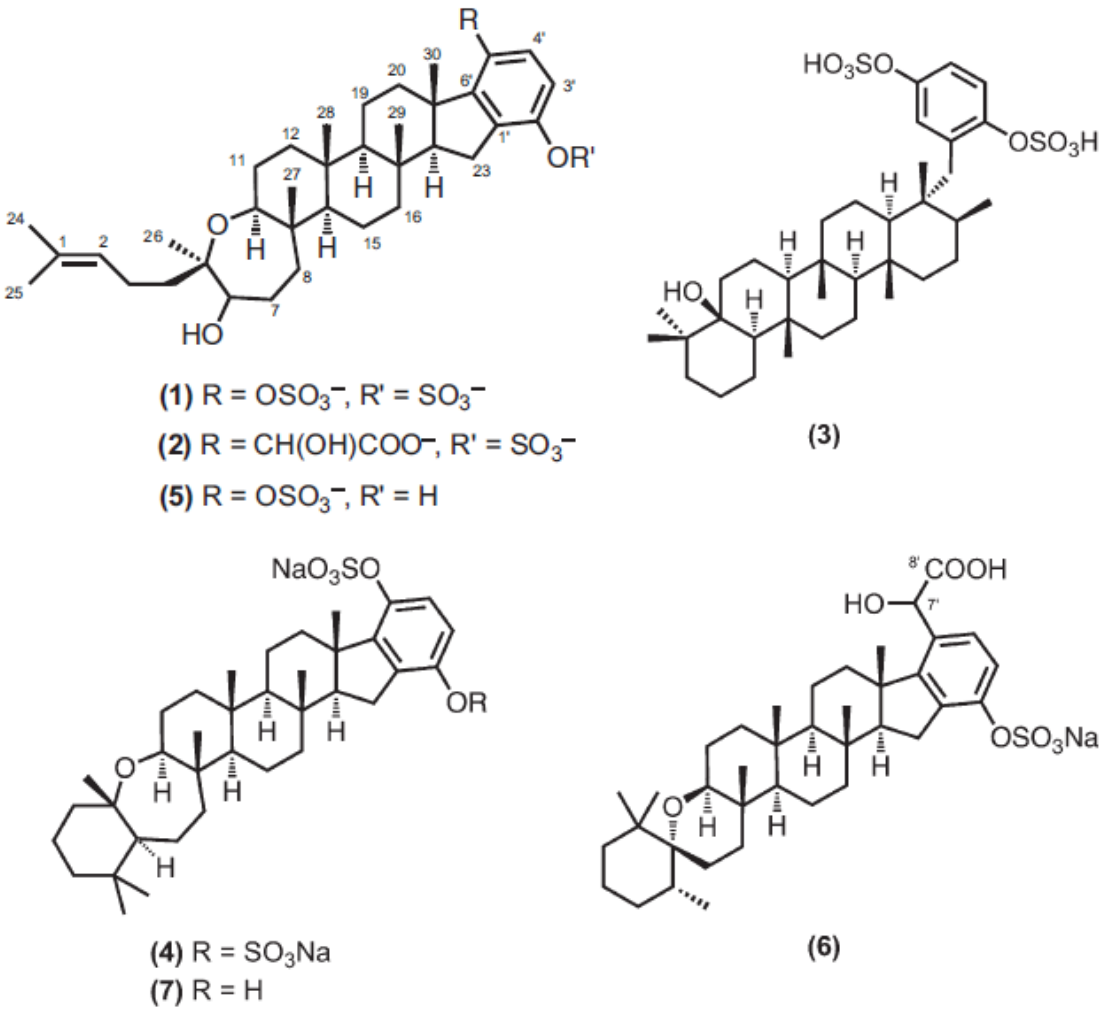

Figure 4.1 Chemical structures of adociasulfates.

AS-10, the sulfate residue at the 5′ position for AS-2 is being replaced by glycolic residue for AS-10, and both of these residues are negatively charged. However, the other parts of the structure of AS-2 and AS-10 are not exactly the same, so one cannot conclude that only the charge of the residue at 5’ matters for AS inhibitory activity.

4.1.2 Two Newly Discovered Adociasulfates

Marine sponges contain a lot of chemical compounds. Our collaborators isolated a few compounds from marine sponge *Cladocroce aculeate* and identified the chemical structure of each compound. They discovered two new compounds that belong to the adociasulfate family. Since there were already 12 AS, the compounds were designated Adociasulfate-13 (AS-13) (**1**) and -14 (AS-14) (**2**) (Figure 4.1). Figure 4.2 shows their structures.

AS-13 and AS-14 have a very similar chemical structure. The only difference is at the 5′ position of the benzylated ring. At this position, it is the sulfate residue for AS-13 and the glycolic acid residue for AS-14. Both residues are negatively charged at neutral pH. Unlike the case of AS-2 and AS-10, AS-13 and AS-14 allow a direct comparison of the function of sulfate residue verses the glycolic residue at the 5’ position.[1]

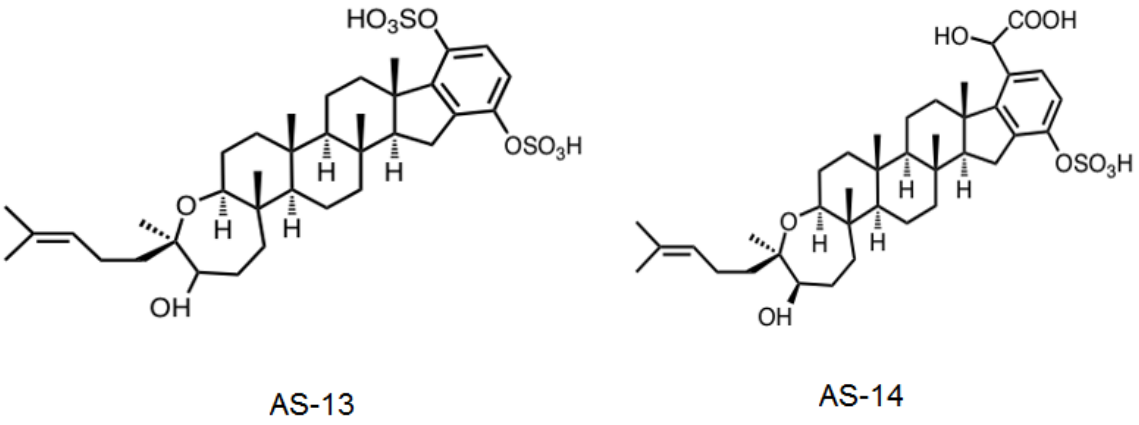

Figure 4.2 Structures of two new adociasulfates: left, AS-13; right, AS-14.

4.2 AS-13 and AS-14 are Strong Inhibitors of Kinesin

I tested whether AS-13 (**1**), -14 (**2**) and -8 (**3**) have similar inhibitory effect on kinesin. I have done this from two different set of experiments.

4.2.1 Kinesin Binding to Microtubule is Inhibited by Adociasulfate

Firstly, I measured the kinesin binding fraction with and without AS. To get this, 1 μm polystyrene beads were preincubated with kinesins, then the beads were brought near MTs via optical trapping and tested for binding activity for 30–40 seconds. The experiment scored the fraction of beads that showed any binding as a function of molar ratio of kinesins to beads at incubation time. In practice, beads concentration was kept the same so the molar ratio was proportional to the dilution ratio for kinesin motors from stock. Previous results showed that AS-2 inhibited kinesin by targeting its motor domain, preventing kinesin from binding to MTs and therefore inhibiting MTs stimulated kinesin ATPase activity. So I tested whether the kinesin binding fraction was less in the presence of the newly discovered AS.

Figure 4.3 shows the binding fractions of kinesins to MTs as a function of relative kinesin concentration. As expected, beads with increasing amount of kinesins per bead showed an increasing binding fraction to MTs. The binding curve can be well fitted to a single molecule Poisson distribution $1 - e^{-x/b}$. Here x is the relative kinesin motor concentration, and b is the effective binding affinity. The lower number the b is, the higher the effective binding affinity.

In the presence of 15 μM AS, the binding fraction curves greatly shift to the right side, meaning the AS dramatically reduced the bead-MT binding. At the kinesin KIF5A dilution K/100000, beads that almost all bound to MTs without AS showed very little binding to

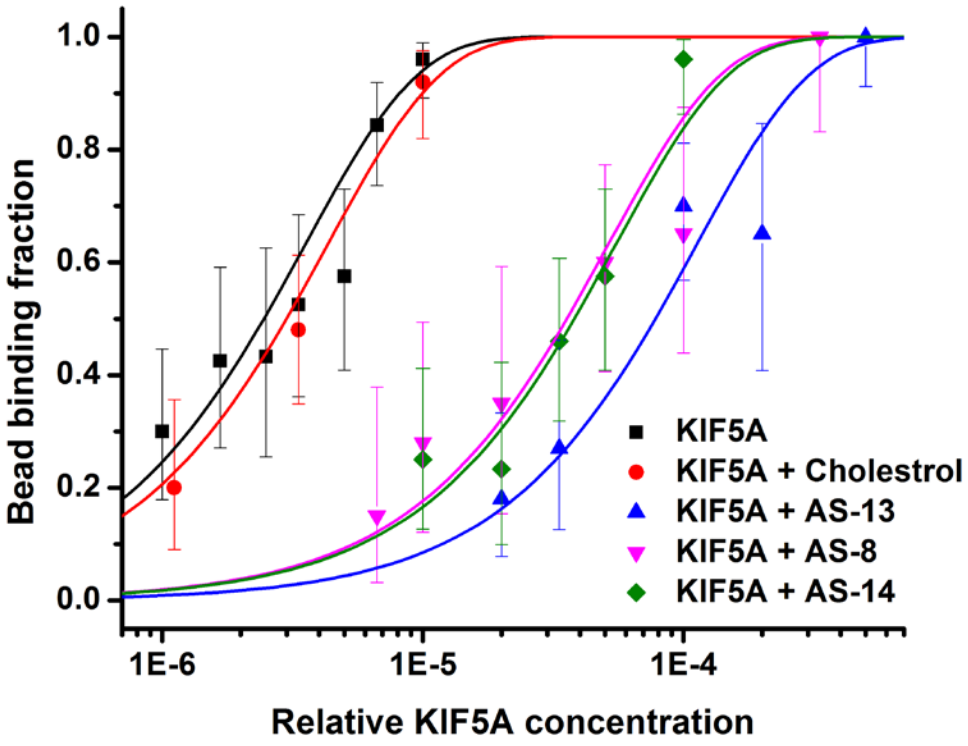

Figure 4.3 Inhibitory effect of AS-8, -13, and -14 on kinesin-MT binding. All binding curves can be well fitted to single molecule Poisson distribution $1 - e^{-x/b}$.

MTs after the addition of 15 μM AS. Beads binding could be rescued by using higher kinesin concentration in the presence of AS. As a control I used cholesterol (Figure 4.4), which has the steroid core structure but lacks the benzylated ring with sulfate residue on it. The fitted effective binding affinities are 3.5e-6 ±0.3e-6, 4.3e-6 ±0.3e-6, 5.1e-5 ±0.9e-5, 5.5e-5 ±0.7e-5, and 1.1e-4 ±0.2e-4 for kinesin alone, kinesin + cholesterol, kinesin + AS-8, kinesin + AS-13, and kinesin + AS-14, respectively. AS-14 and AS-8 showed a similar inhibitory effect on kinesin binding, whereas AS-13 showed the strongest effect. Cholesterol has little effect on kinesin binding.

The half inhibition concentration IC_{50} reported for the strong kinesin inhibitors AS-2, AS-10, and AS-6 varies from 2-6 μM, with full inhibition concentration at 15 μM.[2,3,6] The results showed AS-13 (**1**), AS-14 (**2**), and AS-8 (**3**) are all strong inhibitors for kinesin.

4.2.2 Kinesin's ATPase Activity is Inhibited by Adociasulfate

The single molecule binding experiment directly showed that the new AS significantly inhibit kinesin binding to MTs. So then one would expect the kinesin's MT-stimulated ATPase activity to be inhibited. Since ATP hydrolysis catalyzes the production of ADP

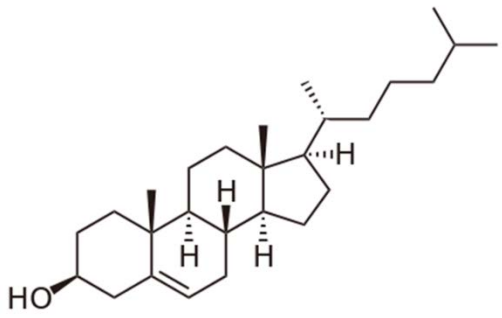

Figure 4.4 Chemical structure of cholesterol.[5] Reprinted from Wikipedia.

and phosphate, the ATPase activity can be monitored by measuring the phosphate amount in the solution.

I used the kinesin's ATPase activity measurement kit (Kinesin HTS ATPase Endpoint Assay, Cytoskeleton, Inc.) by measuring the inorganic phosphate Pi being generated from ATP hydrolysis (Figure 4.5). Kinesins were first mixed with MTs with or without the presence of AS, then ATP was added to the mixture to start the kinesin's ATPase activity. After 5 minutes the reaction was stopped by the addition of stopping buffer. The solution absorbance was measured at 650 nm using a spectrophotometer; higher amounts of phosphate Pi will result in higher numbers of absorbance (Figure 4.5). In the absence of AS, a fairly large amount of Pi was generated; in the presence of 15 μM AS-13, AS-14, or AS-8, no or very little Pi was generated. The absorbance level was close to the blank control, where no Pi was present. Therefore, indeed the kinesin's ATPase activity was significantly inhibited by AS.

These results showed the substitution of one sulfate residue to the negatively charged glycolic acid residue does not eliminate the AS inhibitory effect on kinesin binding to MT.

My findings provide a roadmap for how AS cell permeability can be improved. If one can substitute the sulfate residues with neutral residues so this compound can more easily get into cells, and by some intracellular modification add a negatively charged residue at 5' position of the benzylated ring, then the resulting compound would have an inhibitory effect on kinesin even if the negative residue is not sulfate. In many cells, sulfation is rather uncommon, but other modifications such as phosphorylation are much more prevalent. Therefore my findings increase the value of adociasulfate as a pro-drug candidate.

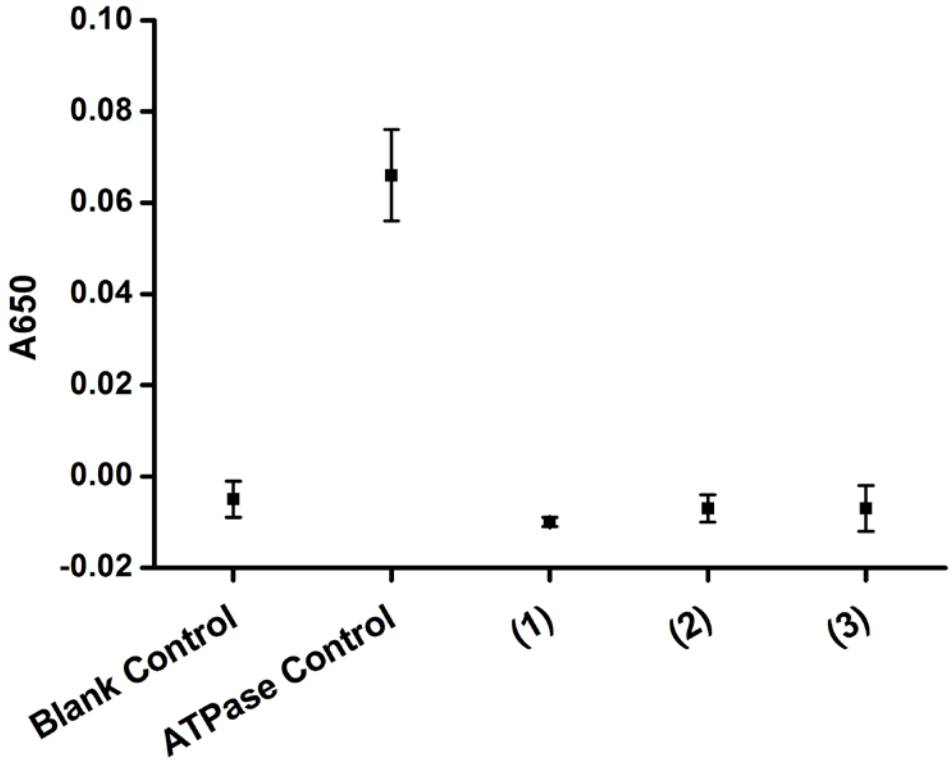

Figure 4.5 Absorbance at 650 nm of inorganic phosphate Pi generated by kinesin's ATPase activity without AS, with AS-13 (**1**), -14 (**2**), and -8 (**3**). Larger absorbance indicates more Pi presence.

4.3 Large Aggregation of Adociasulfates are not Necessary for Inhibition

The mechanism of how AS inhibit kinesin is important for their applications. Large aggregates of AS-2 were observed in solution and proposed to be responsible for kinesin inhibition in a prior study.[7] The study proposed that the rodlike AS aggregates, with the sulfate group exposed to the solution, mimic the negatively charged MTs and thus compete with MTs for kinesin binding.[7]

I tried to detect aggregates of AS in many assays but could not find any. Yet our AS were still strong inhibitors for kinesin. Such experiments do not eliminate the possibility that AS aggregates form under some conditions; however, they do indicate that such aggregates are not required for inhibition. Below I detail the different ways that I searched for the presence of aggregates and how kinesin activity was assayed.

4.3.1 Aggregates Detection from Images

Firstly, our Differential Interference Contrast (DIC) microscope has a high enough resolution to resolve MTs clearly (Figure 4.6), and MTs are only ~25 nm across in diameter. DIC microscopy can typically resolve extended linear structure as small as ~8 nm in cross-section.[9] If there are large aggregates of AS around 200 nm across in diameter, I would be able to view them easily. All surveys of flow chambers revealed no aggregates. However, even if such structures were present somewhere that escaped our inspection, it would not alter our conclusions because kinesin-MT binding was inhibited in all fields of view even though no aggregates were visible.

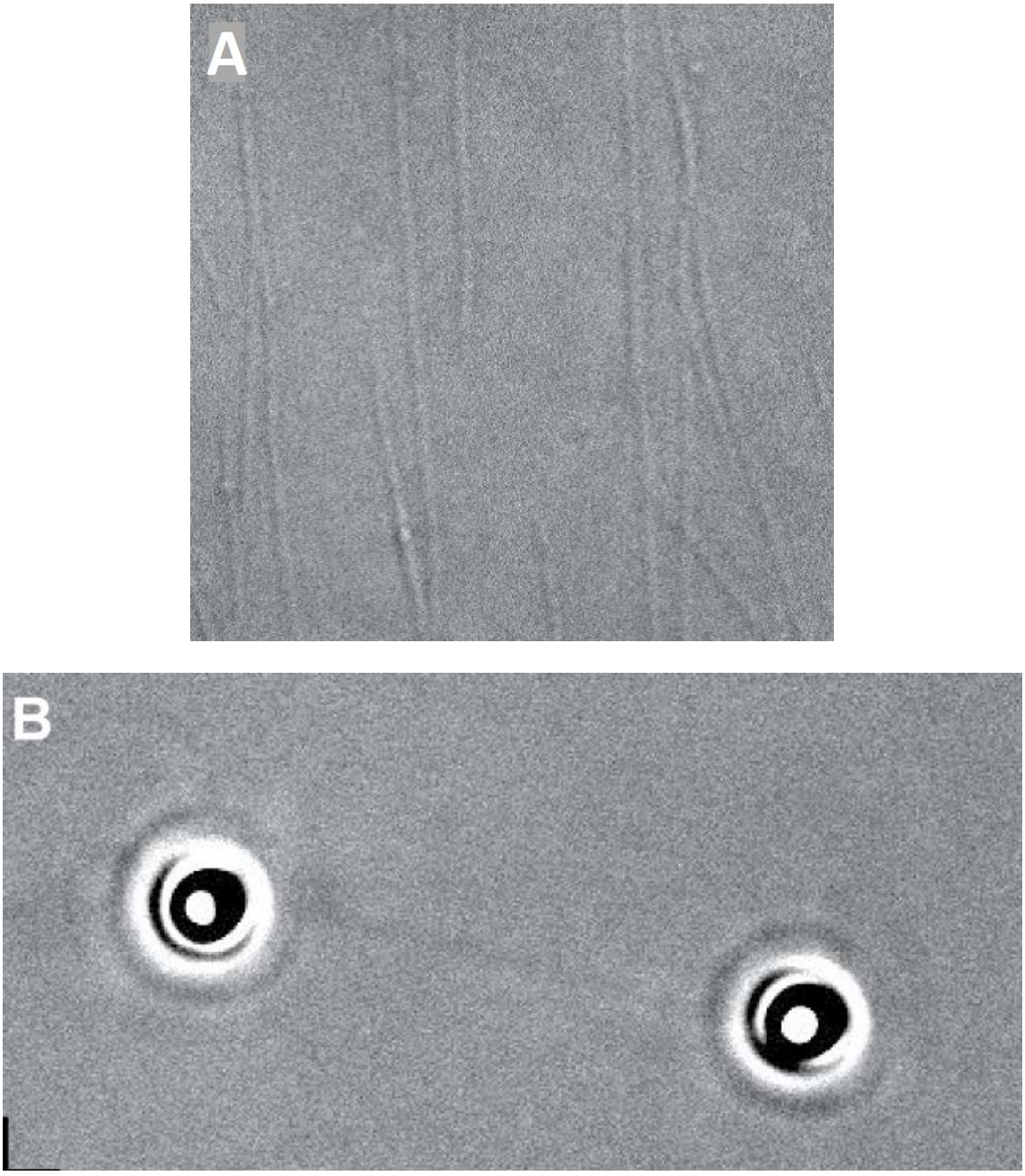

Figure 4.6 Field of view of DIC microscope shows MTs and beads attached to the same MT. A: MT image, MTs can be viewed clearly from our microscope; B: image shows two beads attached to the same MT.

4.3.2 Bead Diffusion Coefficient Measurement

Secondly, to confirm there were no large aggregates of AS, I measured the beads diffusion with and without the presence of AS (Figure 4.7). 1 μm polystyrene beads were diluted in DB (PMEE buffer), with concentration low enough that only one bead was in the field of view so they did not interfere with each other, yet I could still find beads.

According to Stokes-Einstein theory, for Brownian diffusion, the diffusion coefficient can be expressed as

$$\frac{\overline{x^2}}{2t} = D = \frac{k_B T}{6\pi\eta R} \tag{4.1}$$

$\overline{x^2}$ is the mean squared displacement, t is time, D is diffusion coefficient, k_B is Boltzmann's constant, T is absolute temperature, η is dynamic viscosity, and R is the particle radius.

To measure the bead mean squared displacement, beads were incubated with kinesins in DB (viscosity close to water) and then flowed into a flow chamber. One bead at a time were trapped and brought 3 μm above the surface using optical trapping. The bead was then released by turning off the trap, and the video of bead diffusion was recorded using a high resolution video camera (32 frames per second). The bead position in the plane can be analyzed from tracking the bead in the video.

Figure 4.7 shows the mean squared displacement of the bead as a function of time intervals. For all cases, the data can be fitted to a line, indicating essentially pure diffusion. The black line shows fit to data for beads alone. With AS-13 added to the buffer, the mean squared displacement fit line does not significantly change (red line in Figure 4.7).

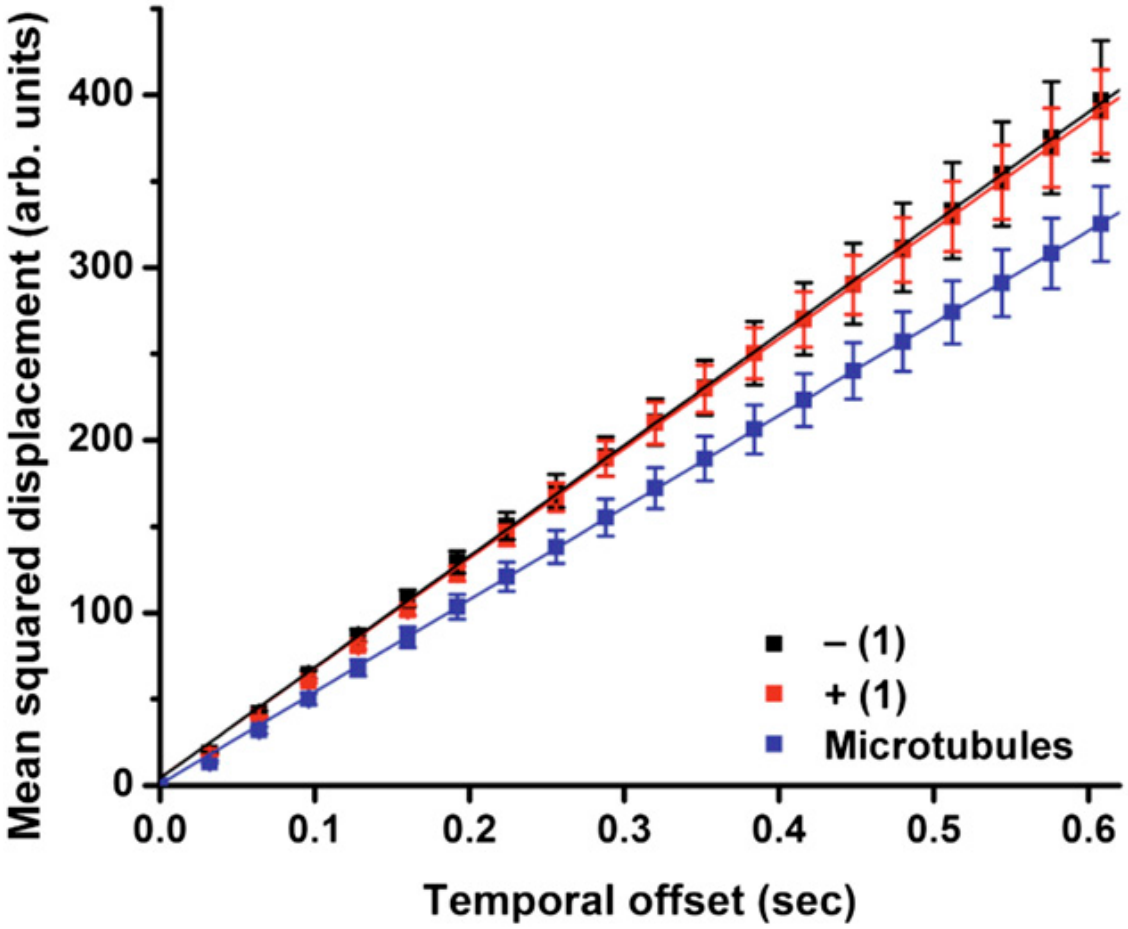

Figure 4.7 Mean squared displacement of beads diffusion.

Therefore beads with pre-adsorbed kinesins show no evidence of extended filaments attached to either the beads themselves or bound to the kinesin motors. For control, the beads were mixed with very short MTs (<1 μm in length) obtained by ultrasonication of MT stock. Here the slope is smaller, indicating a smaller diffusion coefficient D (blue line in Figure 4.7). This is expected because in the absence of ATP, kinesin has strong affinity to MTs, so the MTs would attach to the beads through kinesins, slowing down the bead diffusion.

Neither of these experiments rule out small scale AS aggregation, but they are sufficient to rule out the formation of aggregates comparable or even significantly smaller than those previously reported.

How can one test for the presence of aggregates below 1 μm in size? If there are large aggregates of AS, one would expect more than one bead to bind to the same aggregate. Kinesin heads only occupy 16 nm of linear space on a MT, so aggregates significantly larger than 16 nm would be expected to provide binding space for multiple motors leading to bead clustering. I did not observe bead clustering in any experiment. Control experiments here are simple and numerous. Biotinylated beads can be cross-linked by streptavidin with only four biotin binding sites. Also, of course MTs are an example of a substrate for kinesin with multiple binding sites and indeed, multiple beads are often bound to the same MT (Figure 4.6).

4.3.3 Aggeregates Detection by Turbidity Measurement

Finally, to detect any large aggregate, I did turbidity measurements, which measured the absorbance of AS solutions. The primary value of this measurement is that it measures aggregate formation in a bulk assay not limited to any small field of view under our

microscope. I measured the absorbance at 405 nm (Figure 4.8). This wavelength was chosen as small as possible to improve aggregate detection, but still significantly above the absorption wavelength region of AS. There was no or very little absorbance detected for all the AS buffers (DMSO and motility buffer), indicating no large aggregates were present.

4.4 Adociasulfates and Kinesin Subfamilies

To have an idea of AS inhibition for different kinesin family motors, I tested Eg5 and BimC, in comparison to the conventional kinesin KIF5A used before. Both Eg5 and BimC belong to the kinesin-5 family. They are very homologous; however, BimC contains a second MT binding region at the N terminus end of motor domain [8]. This second MT binding region has ~70 positively charged amino acids and was shown to significantly increase the kinesin binding affinity to MT compared to Eg5.[8]

4.4.1 Inhibition of Mitotic Kinesins by Adociasulfates

I measured the binding fraction curves of Eg5 and BimC with and without AS-13 (Figure 4.9). The binding curve shifted to the right side for both Eg5 and BimC by the addition of 15 μM AS-13, indicating the motors binding to MTs being inhibited. By fitting the binding curve to Poisson distribution function, the effective binding affinities are 0.0117, 0.0266, 0.1502, and 0.3847 for Eg5 alone; Eg5 + AS-13, BimC alone; and BimC + AS-13. By comparing the effective binding affinities, 15 μM AS-13 inhibit Eg5 binding affinity to MTs by 2.3 folder and BimC binding affinity to MTs by 2.6 fold. The inhibition is defined from the effective binding affinity values, and it was plotted in Figure 4.10.

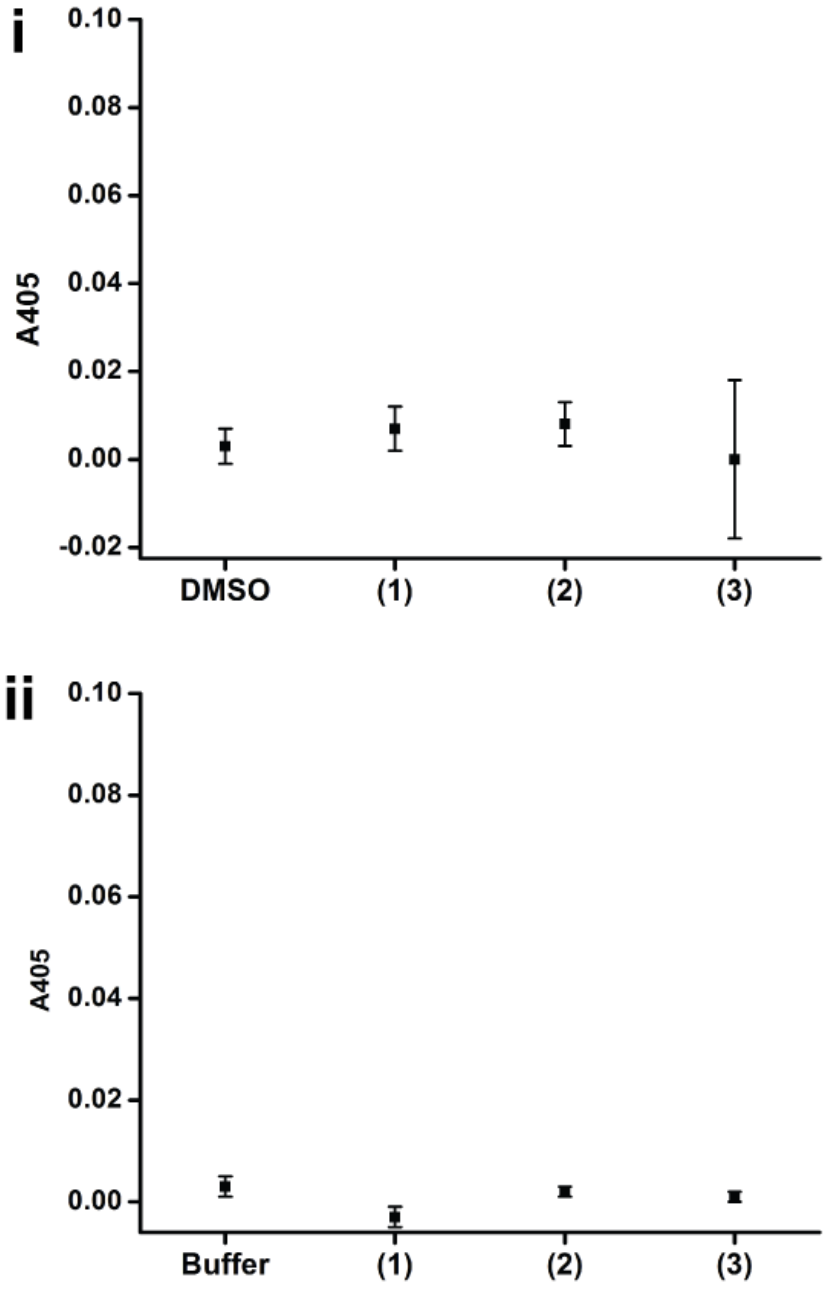

Figure 4.8 Absorbance at 405 nm for AS aggregates detection.

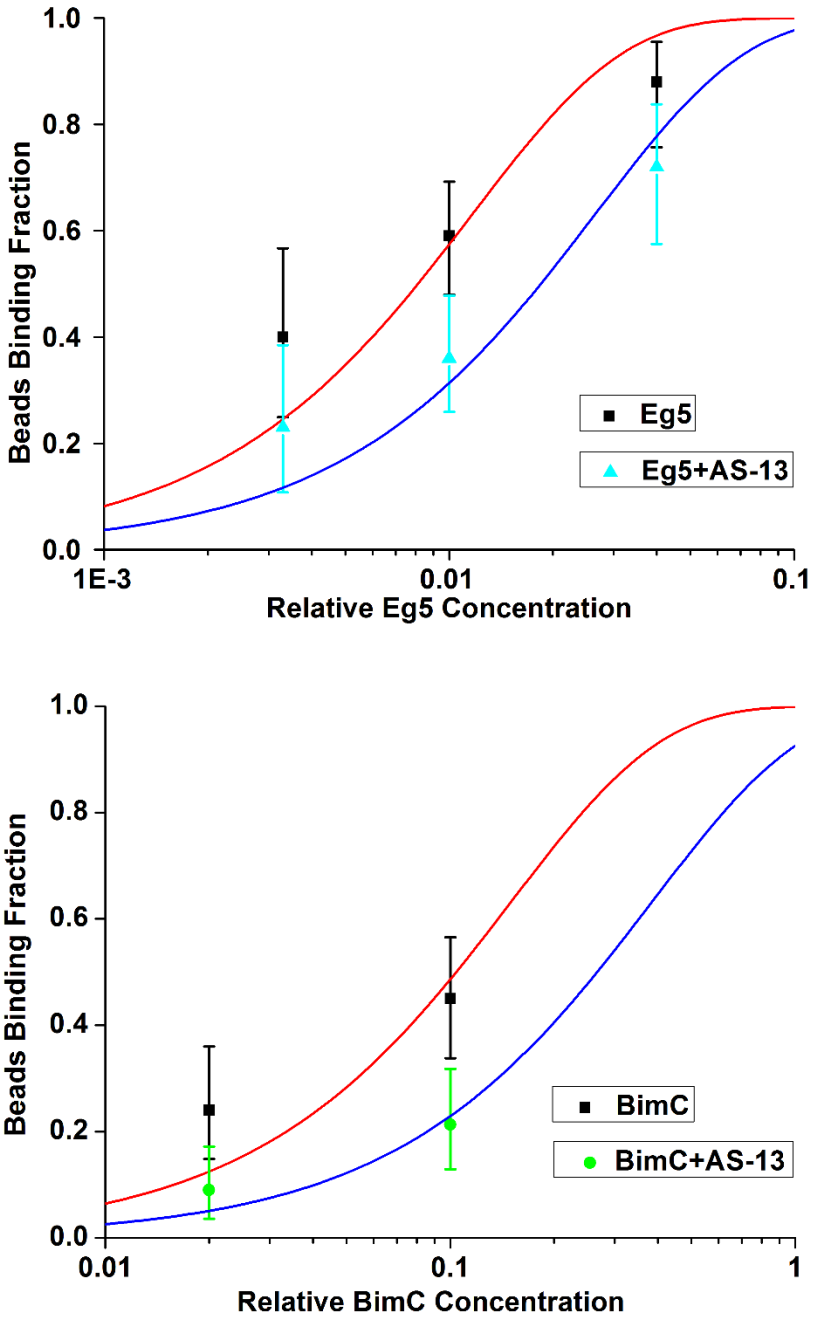

Figure 4.9 Beads binding fraction of Eg5 and BimC. The binding fraction was fitted to single molecule Poisson distribution $1 - e^{-x/b}$.

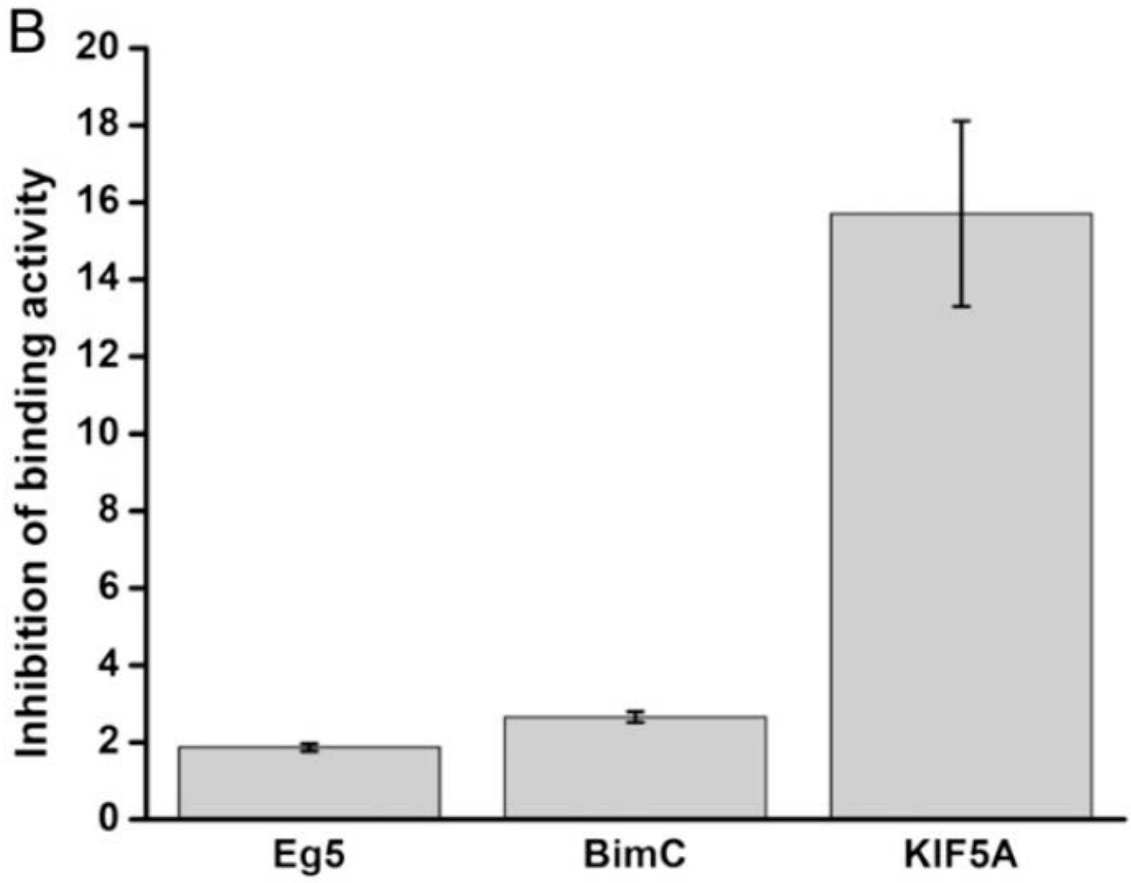

Figure 4.10 Eg5, BimC, and KIF5A inhibition by AS-13.

4.4.2 Comparison of Conventional Kinesin and Mitotic Kinesin

The inhibition of MT binding for mitotic kinesins Eg5 and BimC is much less than that for conventional kinesin (kinesin-1) KIF5A (Figure 4.10). Previous results showed that the IC_{50} value of AS-2 inhibition for kinesin-1 is about 5 times of the value for CENP-E, a mitotic kinesin.[3] I used different sets of kinesin motors and AS and got consistent results. While the testing was not and could not have been exhaustive, it strongly suggests that AS may have much higher inhibition effect on conventional kinesins than mitotic kinesins. Therefore, there exists a window of concentration where AS preferably inhibits conventional kinesins but has little effect on mitotic kinesins.

By comparing the inhibition of the binding activity figure (Figure 4.10), I noticed that AS-13 has comparable inhibition for Eg5 and BimC. Therefore, AS-13 must also inhibit the second BimC-specific MT binding domain. This indicates that AS not only prevents the kinesin motor domain from binding to MT, but also prevents the nonkinesin motor domain from binding to MT. So far, the effect of AS has only been measured for one MT-associated type of motors: kinesins. My data suggest that other motors (dyneins) as well as other microtubule-associated proteins may be affected by AS, and further study is needed to better understand how specific AS activity really is.

4.5 References

[1]. Smith, T. E.; Hong, W.; Zachariah, M. M.; Harper, M. K.; Matainaho, T. K.; Van Wagoner, R. M.; Ireland, C. M.; Vershinin, M. Single Molecule Inhibition of Human Kinesin by Adociasulfate-13 and -14 from the Sponge Cladocroce Aculeate. *Proc. of Natl. Acad. Sci.* **2013**, *110*, 18880–18885

[2]. Blackburn, C. L.; Faulkner, J. D. Adociasulfate 10, a new Merohexaprenoid Sulfate from the Sponge *Haloclona* (*aka adocia*) sp. *Tetrahedron* **2000**, *56* (43), 8429–8432.

[3]. Sakowicz, R. A Marine Natural Product Inhibitor of Kinesin Motors. *Science* **1998**,

280 (5361), 292–295.

[4]. Brier, S., *et al.* The Marine Natural Product Adociasulfate-2 as a Tool to Identify the MT-Binding Region of Kinesins. *Biochemistry* **2006**, *45*, 15644–15653.

[5]. Wikipedia. Cholesterol. http://en.wikipedia.org/wiki/Cholesterol#mediaviewer/File:Cholesterol.svg (accessed Oct 15, 2014).

[6]. Blackburn, C. L., *et al.* Adociasulfates 1–6, Inhibitors of Kinesin Motor Proteins from the Sponge Haliclona (aka Adocia) sp. *J. Org. Chem.* **1999**, *64* (15), 5565–5570.

[7]. Reddie, K. G.; Roberts, D. R.; Dore, T. M. Inhibition of Kinesin Motor Proteins by Adociasulfate-2. *J. Med. Chem.* **2006**, *49* (16), 4857–4860.

[8]. Stock, M. F.; Chu, J.; Hackney, D. D. The Kinesin Family Member Bimc Contains a Second Microtubule Binding Region Attached to the N Terminus of the Motor Domain. *J. Biol. Chem.* **2003**, *278* (52), 52315–52322.

[9]. Stemmer, A. Individual Actin Filaments Visualized by DIC (Nomarski) Microscopy. *Biol. Bull* **1992**, *183*, 360–361.

CHAPTER 5

THE EFFECT OF TEMPERATURE ON MOLECULAR MOTORS' ACTIVITY

5.1 Introduction

Organelles and vesicles in cells often move bidirectionally. Significant evidences have recently accumulated to suggest that in many cases both kinesin and dynein motors are present on the same cargo.[9] Kinesins usually move cargos to the plus end of MTs while dyneins move cargos to the minus end. The mechanisms regulating cargo transport while keeping it in homeostatic balance are still not fully understood.

Cells can survive in a wide range of temperature, as much as ~40 °C in cells of heterotherm and poikilotherm animals. Clearly these cells still function normally at different temperatures, which (in eukaryotes) require functional MT-based transport. A critical question then is how the temperature affects the regulation and balance of motor activity in cells. To understand such a complex system, one must start from examining and modeling individual motor activity to provide a basis for building complexity *in vitro*.

Furthermore, understanding the thermal balance of molecular motor transport will provide useful information for nanotechnology applications. This is because MT-based transport is an attractive technology for many nanotech designs,[11] but one of the main challenges is the stabilization of the transport in such devices under temperature changes.

5.2 Tug-Of-War Introduction

Kinesin and dynein motors move cargos (vesicles, organelles, proteins and mRNA compexes) in opposite directions along MTs. *In vitro* studies showed that while a single kinesin or dynein motor will fall off from MTs after about 1 μm of movement and generate a small force (kinesin stall force around 5 pN and dynein stall force aroud 1 pN), two or more motors can move cargos much longer distances and can generate relatively high forces. Thus to move large cargos *in vivo* processively for long distances, multiple motors must work together (although in some cases processivity of individual motor can be boosted by regulation). The tug-of-war between multiple kinesin and dynein motors is a complex phenomenon whose details are not yet fully understood.

A great, highly informative example of bidirectional transport is provided by the recent work of the Mallik lab. Figure 5.1 shows the movement of *Dictyostelium* endosomes on polarity-labeled MTs.[10] The endosome with both kinesin and dynein motors bound to it starts to move in one direction, then it switches directions, with slow movement with lots of reversals in between due to tug-of-war (TOW). During the TOW, the trace almost always has a slope, meaning the velocity of cargo is not zero, and this indicates one part of the motors winning the TOW. For the two TOW cases in Figure 5.1, the velocity is negative, indicating dynein winning.

5.3 Arrhenius Equation

It is typically the case that enzymatic chemical reactions happen faster at higher temperatures. The Arrhenius equation often accurately describes the temperature dependence of the chemical reaction rate. The Arrhenius relationship states

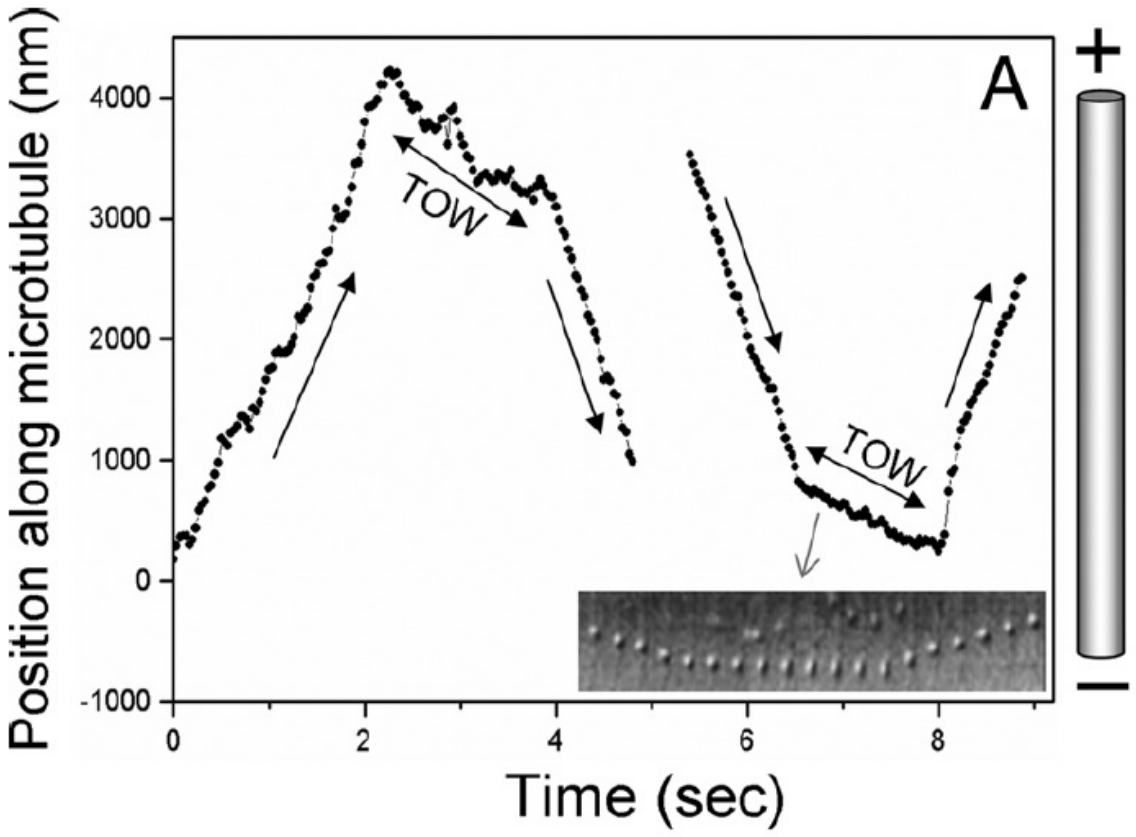

Figure 5.1 Motion of endosome on MTs. Between the unidirectional movements, there is tug-of-war (TOW) movement. Figure from reference [10]. Reprinted with permission from PNAS.

$$k = Ae^{-\frac{E_a}{RT}} \tag{5.1}$$

Here k is the chemical reaction rate, A is constant, R is the universal gas constant, T is absolute temperature, and E_a is activation energy.

Here, activation energy refers to the height of an energy barrier that separates the starting reactant and product states of the system (Figure 5.2).

Kinesin and dynein motors are chemical enzymes that hydrolyze ATP to ADP and phosphate (Pi). One may expect that the ATP hydrolysis rate should follow the Arrhenius relationship. Kinesin is a strongly-coupled motor and produces 1 step per 1 ATP hydrolyzed. Therefore, velocity should then also follow a simple Arrhenius relationship.

Indeed, the velocity measurements for kinesin between 15 °C and 35 °C can be fitted

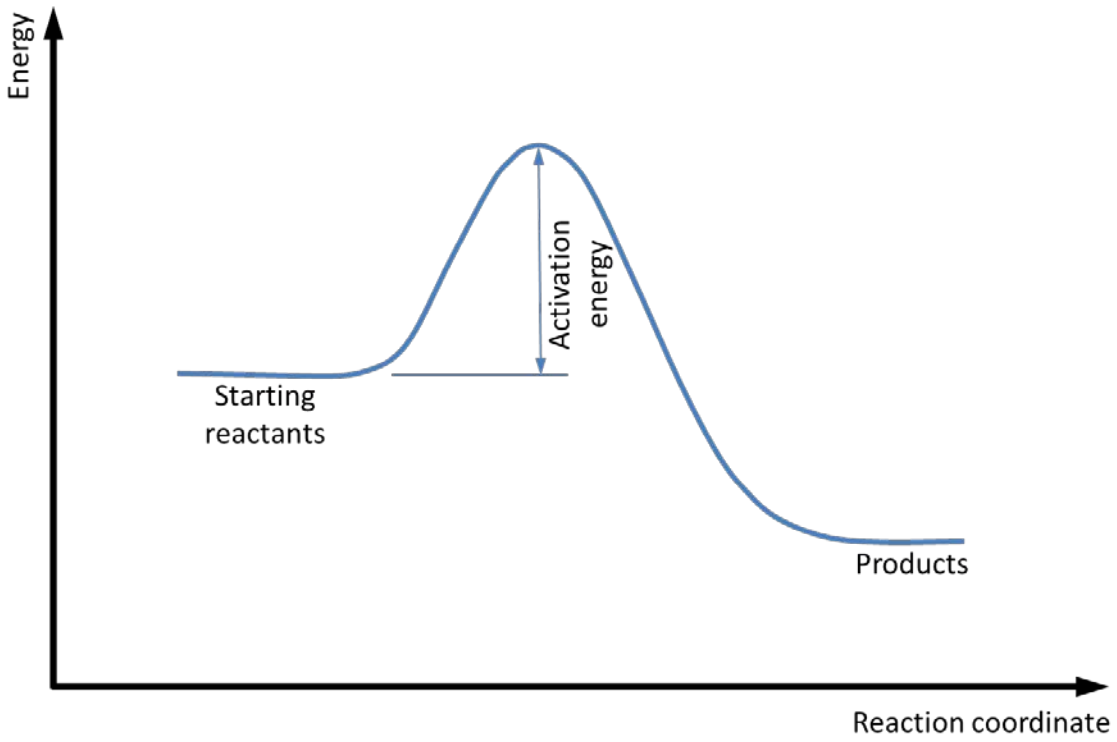

Figure 5.2 Arrhenius temperature dependence of enzymatic rate.

to the Arrhenius plot.[1] The mechanochemical coupling of dynein is more complex, but if this coupling is temperature-independent, then one may still expect a simple Arrhenius relationship for velocity.

For motor velocities, the Arrhenius relationship should be

$$V = V_0 e^{-\frac{E_a}{RT}} \tag{5.2}$$

Here V is motor velocity. To get the activation energy E_a, it is easiest to take the logarithms of the above equation and rearrange the equation as

$$In\, V = In\, V_0 - \frac{E_a}{RT} \tag{5.3}$$

which states that the logarithm of velocity $ln\, V$ is linear with the inverse of temperature $\frac{1}{T}$. The slope of the plot would be $-\frac{E_a}{R}$; thus the activation energy can be easily calculated from the slope of this plot.

5.4 Kinesin and Cytoplasmic Dynein are Processive in Bead Assays

In cells, kinesin-1 and cytoplasmic dynein can move many steps without detaching, which is described as "processive." With no cargo attachment, kinesin and dynein are inactive, in a self-inhibited conformation. Cargo binding can activate the motor. However, recent studies showed that single cytoplasmic dynein may need dynactin, and one additional adaptor protein that links to the cargo to become processive *in vitro* and likely also *in vivo*.[3] Otherwise it may need more than one motor working together to reliably move an appreciable distance.[3] So to study dynein *in vitro*, I needed to first reexamine

whether single cytoplasmic dynein can be active and processive when just attached to polystyrene beads. Figure 5.3 shows the bead binding fraction as a function of relative dynein concentration (the procedure for binding fraction measurements of motors has been described above for kinesin). The binding fraction can only be fitted to a single motor Poisson distribution $1 - e^{-x/b}$, not two $1 - e^{-\frac{x}{b}} - \frac{x}{b}e^{-x/b}$ (dashed line fit), or more motors distribution (dotted line fit) (Figure 5.3). This indicates that cytoplasmic dynein can work alone to be processive. Indeed, when the bead binding fraction is below 0.3 (single motor limit),[5] processive movement was still observed.

It has been long known that single kinesin is processive, and no recent findings question this fact. I still confirmed this by measuring the bead binding fraction of kinesin, and it can indeed be fitted to a single motor Poisson distribution (Figure 5.4).

5.5 Molecular Motor Velocity Dependence of Temperature

I measured kinesin and cytoplasmic dynein motor velocities in a wide range of temperatures (Figure 5.5). The velocity was fitted to the Arrhenius equation $V = V_0 e^{-\frac{E_a}{RT}}$.

As expected, the motor velocities decrease as the temperature decreases. However, dynein velocity showed piece-wise Arrhenius behavior. That is, the velocity data can be fitted to more than one Arrhenius equation.

5.5.1 Kinesin Velocity Dependence of Temperature

For kinesin the velocity was measured from 27 °C to -8 °C and showed Arrhenius behavior (Figure 5.5a). The activation energy is ~65 kJ/mol, relatively consistent with previous work,[1] though prior results were for a different kinesin-1 isoform (KIF5B). Kinesin was shown to degrade above 27 °C;[6] however, if I measure the kinesin velocity

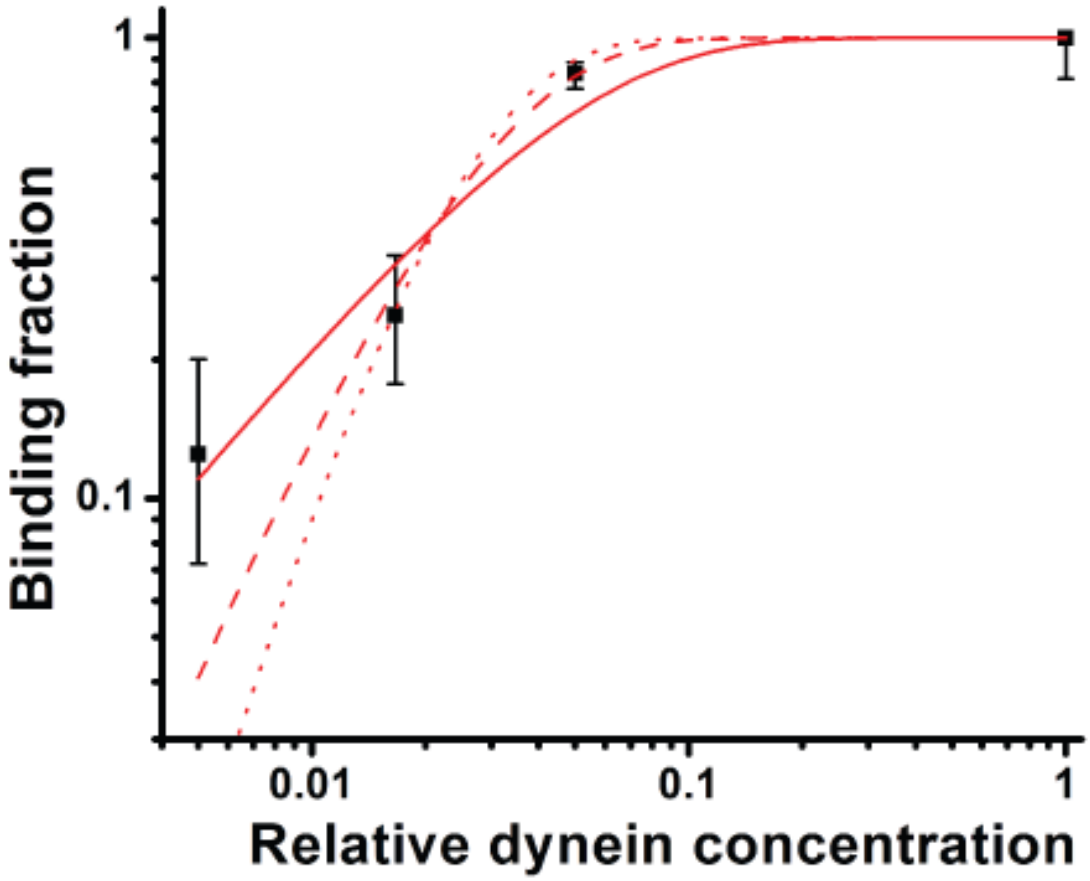

Figure 5.3 Cytoplasmic dynein binding fraction as a function of relative concentration.

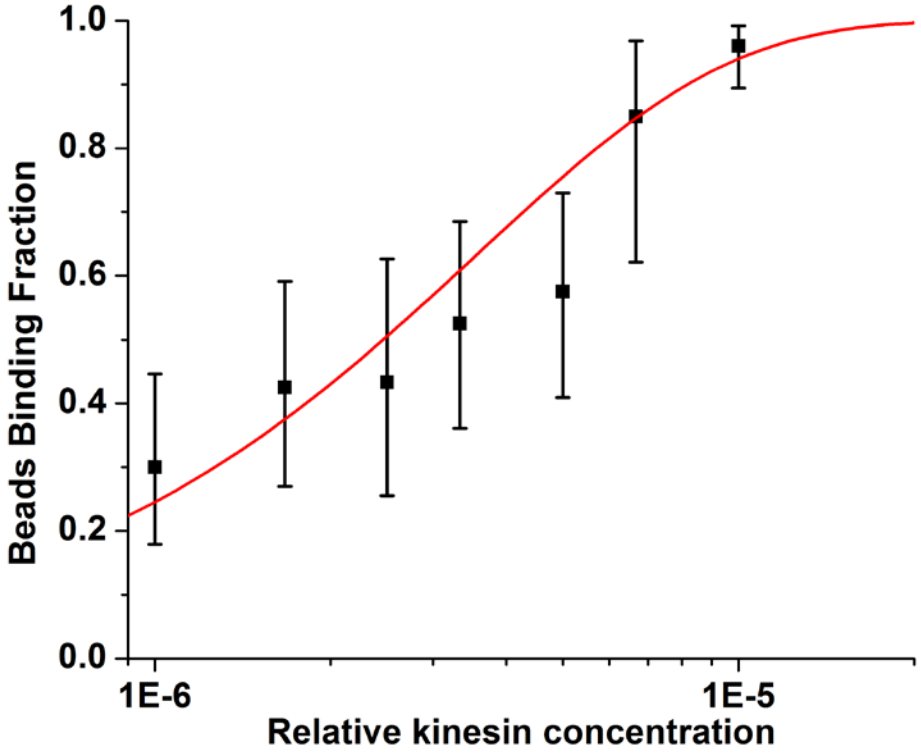

Figure 5.4 Kinesin-1 binding fraction as a function of the relative concentration.

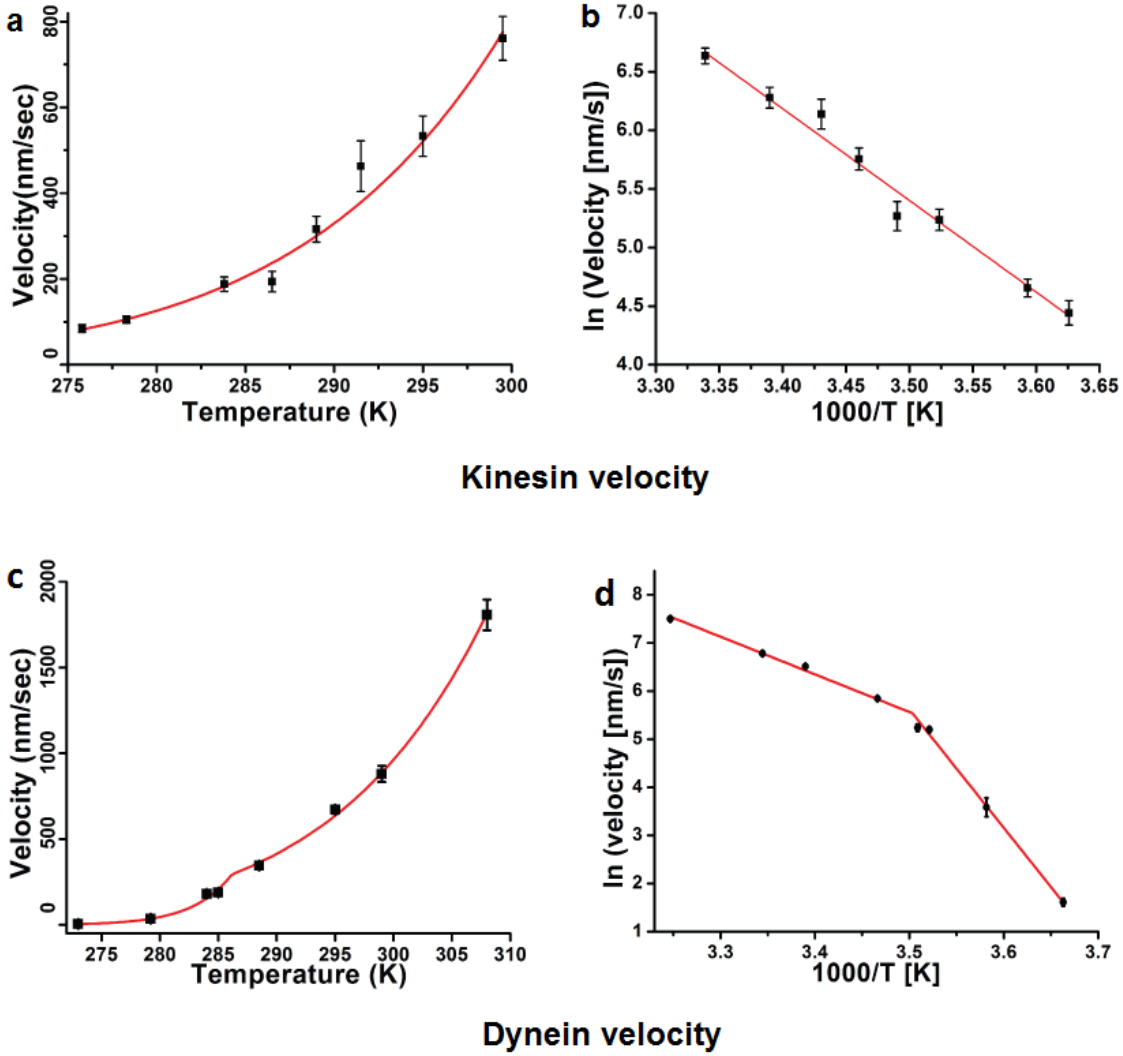

Figure 5.5 Kinesin and dynein velocities change as function of temperature. a: kinesin velocity changes with temperature, the velocity data were fit to the Arrhenius equation; b: logarithm plot of kinesin velocity over temperature; c: dynein velocity changes with temperature, the velocity data were fit to the Arrhenius equation; d: logarithm plot of dynein velocity over temperature.

within 10 minutes after raising temperature up to 37 °C, there is still kinesin movement, and the velocity still follows the Arrhenius trend even at high temperatures. After 10 minutes, there are more and more kinesin beads stuck to MTs, which suggests motor degradation. The experimental approach of measuring motor velocity soon after raising the temperature is very similar to temperature pulsed microscopy developed by the Ishiwata lab, and my observations for KIF5A reproduce their results closely. The reason why kinesin works normally at 37 °C in cells, but degrades *in vitro* at that temperature is not known and is worth investigating in the future.

It is worth mentioning that the kinetics of ATP binding to myosin was studied, and a break at 13 °C for the Arrhenius plot was observed.[2] This break was attributed to the transition of the rate-limiting step.[2] Since kinesin and myosin likely evolved from the same ancestor protein,[4] they share a great structural similarity within the motor domain, especially within the ATP binding pocket.[7] It is interesting that previous studies showed that kinesin has two steps in the enzymatic cycle that are close to being rate limiting.[8] I thus expect that the Arrhenius plot for kinesin would also shows piece-wise linear character, but this is not seen down to 8 °C.

5.5.2 Dynein Velocity Dependence of Temperature

For dynein velocity, I measured a temperature range from ~36 °C to 0 °C (Figure 5.5b). The velocity data can be fitted to two Arrhenius decays, with the break at ~15 °C. At temperatures above ~15 °C, the corresponding activation energy is ~71 kJ/mol, close to kinesin-1 in this temperature range. The fact that the dynein velocity above 27 °C fits to the Arrhenius equation indicates dynein is thermally stable at high temperatures. Since the velocities of kinesin-1 and dynein are close to each other at room temperature, it is natural

to speculate that their velocities would be also matched up to 37 °C, assuming kinesin is thermally stabilized *in vivo*. At temperature below 15 °C, dynein velocity drops quickly to ~5 nm/s, and the corresponding activation energy is ~ 196 kJ/mol, significantly higher than ~71 kJ/mol.

5.5.3 Cause for Arrehnius Break

There are three main causes one can propose for the observed break of the Arrhenius plot.[2] One is that the step in the enzymatic cycle that was rate limiting at high temperatures is no longer limiting at low temperatures. If a different energy barrier becomes dominant at low temperatures, then the slope of the Arrhenius plot can change too.

The other cause for the break of the Arrhenius plot is the structural change of the enzyme due to the temperature change. When the temperature drops, the whole structure of the motor may change dramatically at some temperature, which may change the stepping behavior.

Finally, both cytoplasmic dynein and kinesin-1 are dimeric motors. Therefore it is possible that even though the ATPase rate of each motor domain has the same Arrhenius trend for its activity at all temperatures, the mechanical stepping is inhibited due to a change in motor coordination between heavy chains.

The force measurement of dynein (Figure 5.6) shows no difference at temperatures above and below the break. This measurement hints that there is no significant structural change of dynein at the break. Also, it is hard to see how dynein could degrade at lower temperatures since protein degradation usually occurs at high temperatures. Therefore, changes in the enzymatic cycle or in interhead coordination appear to be the likeliest candidates for the observed effect. We also measured the velocity of yeast dynein and

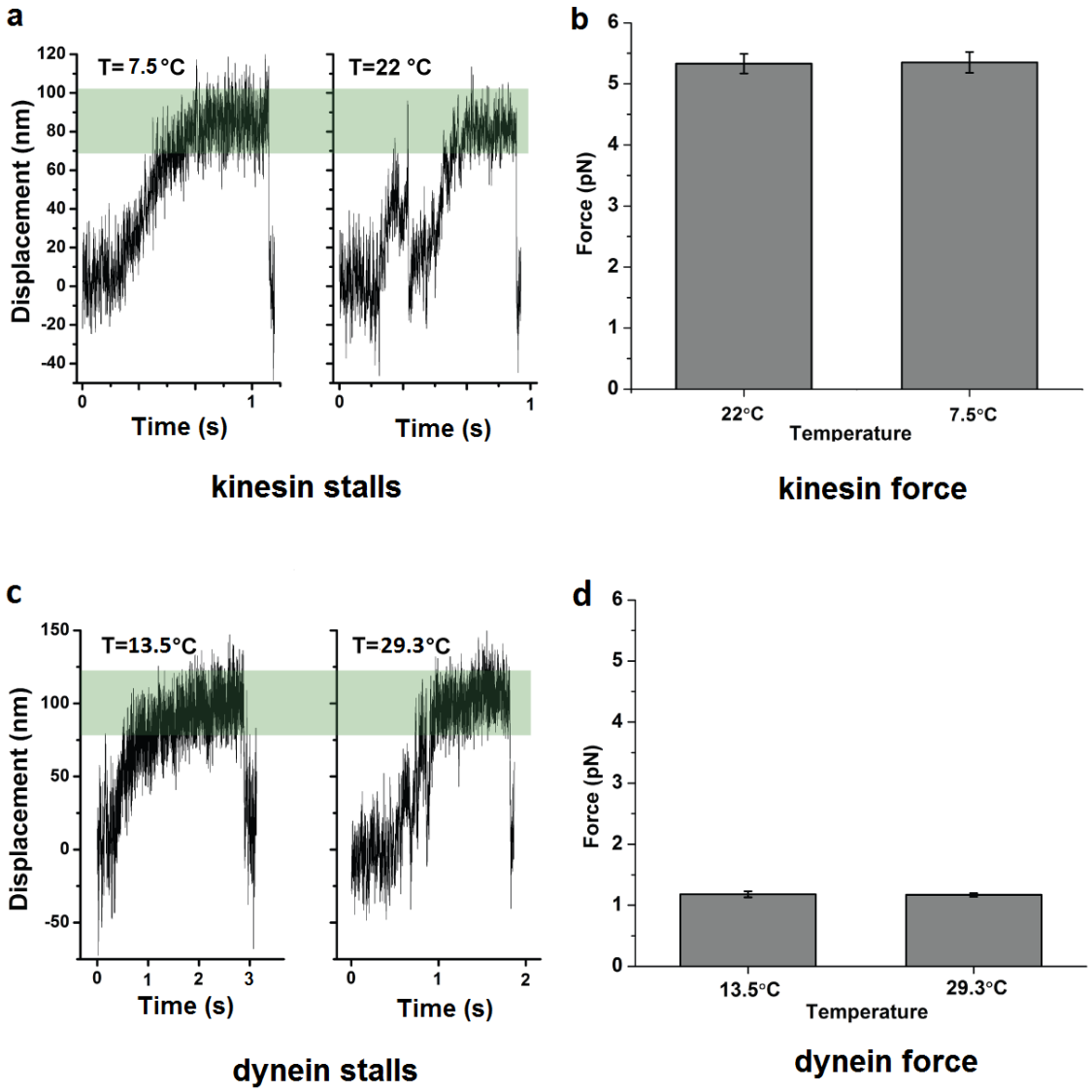

Figure 5.6 Kinesin and dynein force measurements at different temperature. a: kinesin force. a: bead traces show one kinesin stall at around 90 nm displacement at 7.5°C and 22°C; b: kinesin forces at 7.5°C and 22°C show no significant difference; c: bead traces show one dynein stall at around 115 nm displacement at 13.5°C and 29.3°C; b: kinesin forces at 13.5°C and 29.3°C show no significant difference.

plotted the Arrhenius decay, and found that yeast dynein also showed an Arrhenius break at ~10 °C. Cytoplasmic and yeast dyneins have different structure, and therefore it is unlikely that their interhead coordination change the same way at low temperature. So we conclude the Arrhenius break for dynein is from the change in the enzymatic cycle.

5.6 Kinesin and Cytoplasmic Dynein Force Dependence of Temperature

Force measurements in bead assay require the ability to monitor bead position with high spatial precision and small time steps. Our system has a quadrant photo diode (**QPD**) installed (Figure 1.1); however, for this work I used a high speed USB3 camera (Ximea MQ003MG-CM). The camera can image a single line on a sensor at ~8.8 kHz rate, but for practical region of interest sizes can only be driven as fast as 4000 fps (frames per second). This is enough for force measurements and has many advantages over the **QPD**. The **QPD** can only measure small displacement of the particle near the trap center precisely; the Ximea camera, on the other hand, does not involve laser tracking and can measure the particle position in the whole field of view precisely. The Ximea camera also enables fast measurement of particle position without the need of a condenser to contact the sample. With the condenser being above the sample, the illumination for such experiments is sufficient for MT imaging. The advantage of this setup is that for temperature-related measurements, the condenser no longer acted as a heat sink (or source) for the flow cell, which greatly improved the temperature control in the sample.

To get single molecule stall force, I used motor concentration at which the beads binding fraction is 30%. Statistically this ensures the bead that moves has only one motor

bound to it.[5] Figure 5.6 shows recorded beads position when beads move and stall. At first, when the bead was trapped and brought near a MT, the bead Brownian motion around the trap center was limited by the trapping potential of the laser trap. Once the motor bound to MT, it started to move along the MT. Here the displacements are below 120 nm, so the restoring force exerted on the bead by the trap is proportional to its displacement from the trap center.[5] When the bead moved further away from the trap center, the restoring force got larger so that eventually the bead motion slowed and then came to a stall. At this point, the force the motor exerted on the bead balanced the restoring force, and this force is usually called the stall force. To avoid counting fluctuations, I only counted those traces where the bead stayed at the plateau (stall) for at least 0.3 second.

5.6.1 Kinesin Force Variation with Temperature

For kinesin, I measured the single molecule stall force at 7.5 °C and 22 °C (Figure 5.6a). The average force is 5.30 ±0.17 pN at 22 °C and 5.25 ±0.15 pN at 7.5 °C. The force histogram can be fitted to the Gaussian distribution at both temperatures (Figure 5.7). I performed a t-test to compare these two sets of data, and there are no differences between them. This result confirms and extends the previous result by Isiwata lab.[1]

5.6.2 Dynein Force Variation with Temperature

For dynein, I measured the single molecule stall force at 13.5 °C and 29.5 °C (Figure 5.6b). The average force is 1.17 ±0.03 pN at 29.5 °C and 1.18 ±0.05 pN at 13.5 °C. T-test shows no difference between the data at different temperatures. Remember the break of the Arrhenius plot occurs at ~15 °C.

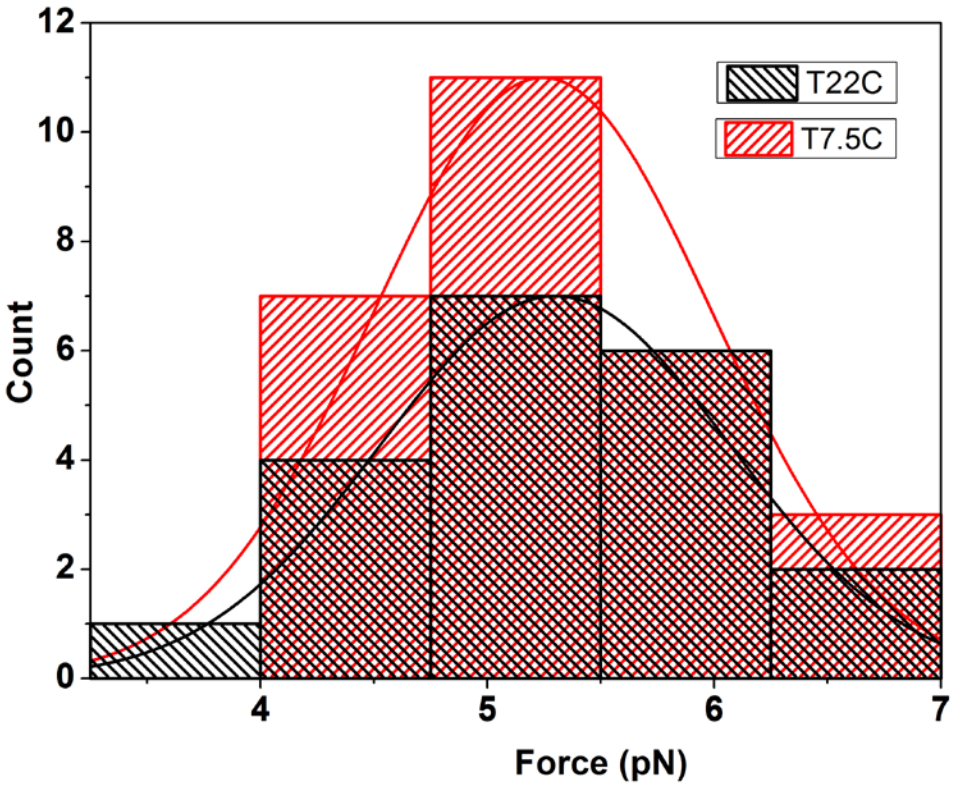

Figure 5.7 Kinesin force distribution histogram.

It is hard to get stall forces at low temperatures due to the slow motor motion, so I chose the temperatures above and below the Arrhenius break, yet the temperature at which the motor velocity is still high, so it is possible to do the experiment.

Should one expect to see differences in stall forces? The energy scale change at this temperature range ($\Delta\kappa_B T$ ~0.2 pN·nm) is much smaller than the energy scale for stepping near stall force (kinesin ~45 pN·nm and cytoplasmic dynein ~10 pN·nm). Without some structural change (degradation or refolding), the thermal energy change is likely too small to produce a measurable stall force change. So these results are not surprising but provide indirect evidence that kinesin and dynein have no significant structural change in this temperature range.

5.7 Implication for Bidirectional Movement

The difference between velocity behavior of dynein and kinesin makes the question of what happens to bidirectional transport as a function of temperature very interesting. So how do single molecule properties affect the ensemble motors movement?

My results reveal a significant transition for dynein velocity at 15 °C. Below this temperature, kinesin velocity drops relatively slow while dynein velocity drops quickly (Figure 5.8). At room temperature, kinesin and dynein have comparable velocities (kinesin 533 ±47 nm/s, dynein 672 ±23 nm/s), and this comparable velocity holds until 15 °C (kinesin 315 ±30 nm/s, dynein 345 ±2 nm/s). Below 15 °C, kinesin and dynein velocities deviate quickly. At 5 °C, kinesin velocity is almost one order of magnitude higher than dynein velocity (kinesin ~105 nm/s, dynein ~25 nm/s) (Figure 5.8).

To explore this effect on bidirectional transport, our collaborators use their well-established simulation model to simulate the motility when a cargo is pulled by multiple

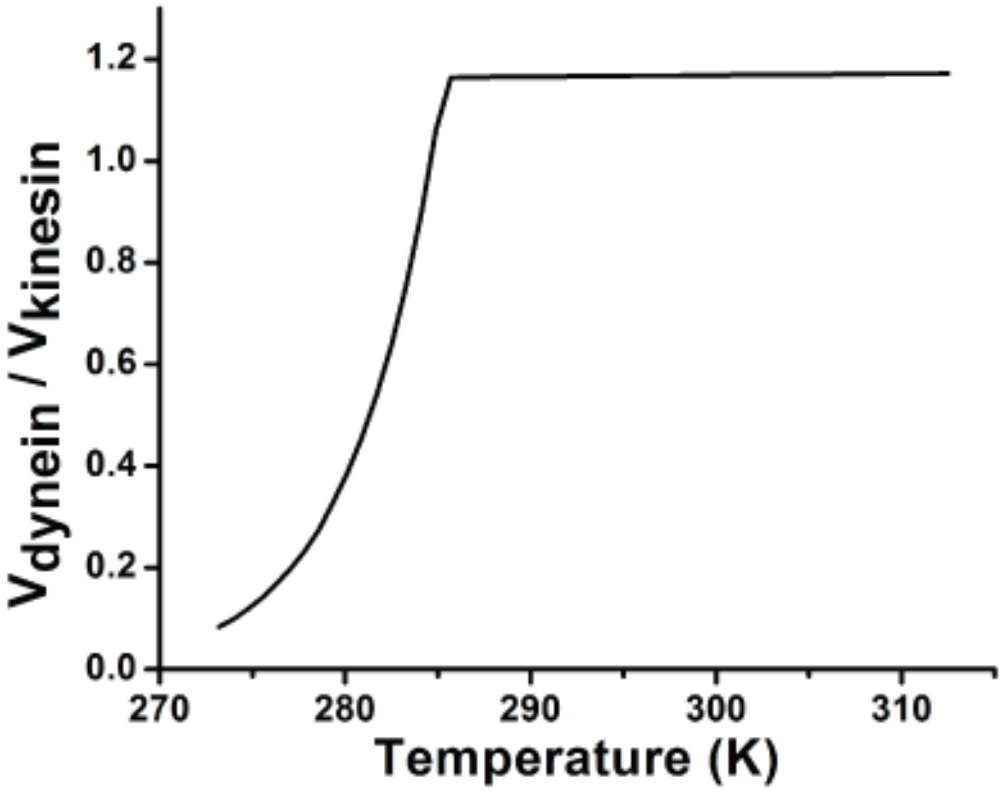

Figure 5.8 Ratio of dynein to kinesin velocities varies with temperature.

kinesin and dynein motors. Consider a cargo that is driven by one kinesin-1 and four cytoplasmic dynein motors (Figure 5.9). The forces are close to balanced. Each motor has an on- and off- rate, which is determined from previous experiments, and each motor can take steps stochastically. The simulation ends when the bead falls off the MT when all motors are unbound at the same time.

Figure 5.10 shows the bead traces along MT at different temperature. At the temperature around the Arrhenius break 287–288 K (~14–15 °C), most beads move toward the minus end of MT, indicating dynein wins the tug-of-war. However, at low temperatures below the Arrhenius break, e.g., 274 K (~2 °C), kinesin wins the tug-of-war.

Figure 5.11 shows the probability of kinesin and dynein winning the tug-of-war

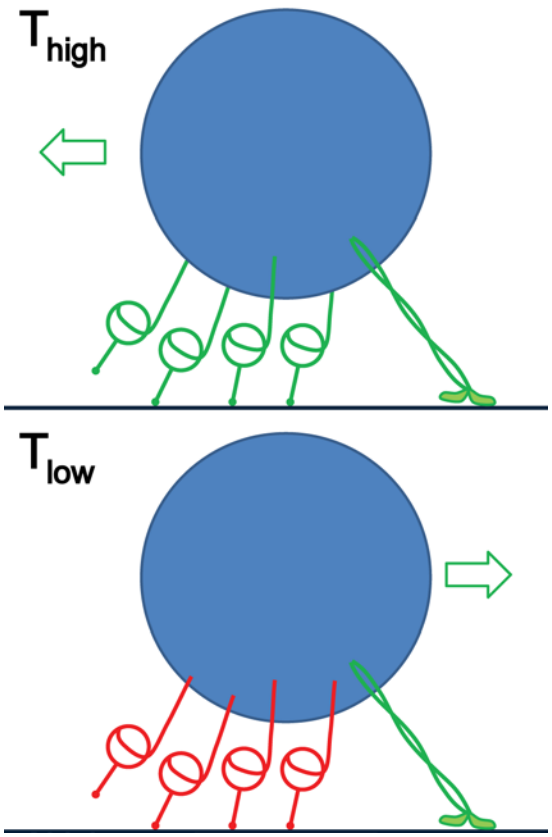

Figure 5.9 Cartoon model of simulation. One bead with one kinesin and four dynein motors bound to it. The black line is the MT.

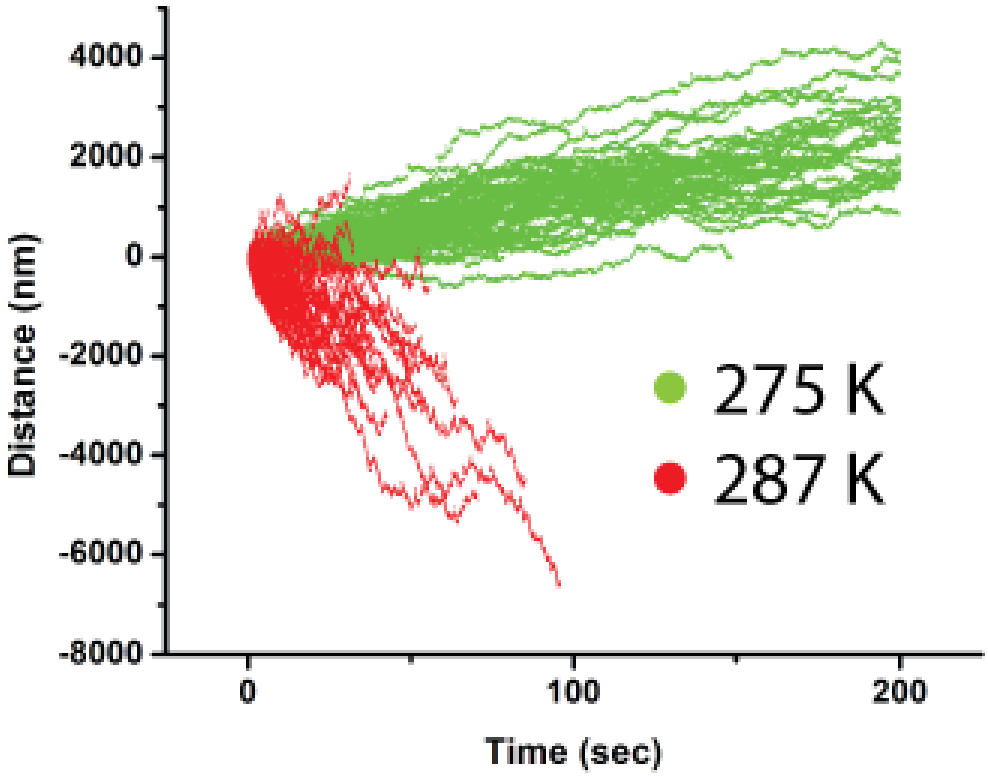

Figure 5.10 Simulated bead traces along MT. Red is the trace at high temperature above the Arrhenius break, and green is the trace at low temperature below the break. Distance at 0 is the position the bead starts to move. Positive and negative distance are the movement toward the plus- and minus-end of MT.

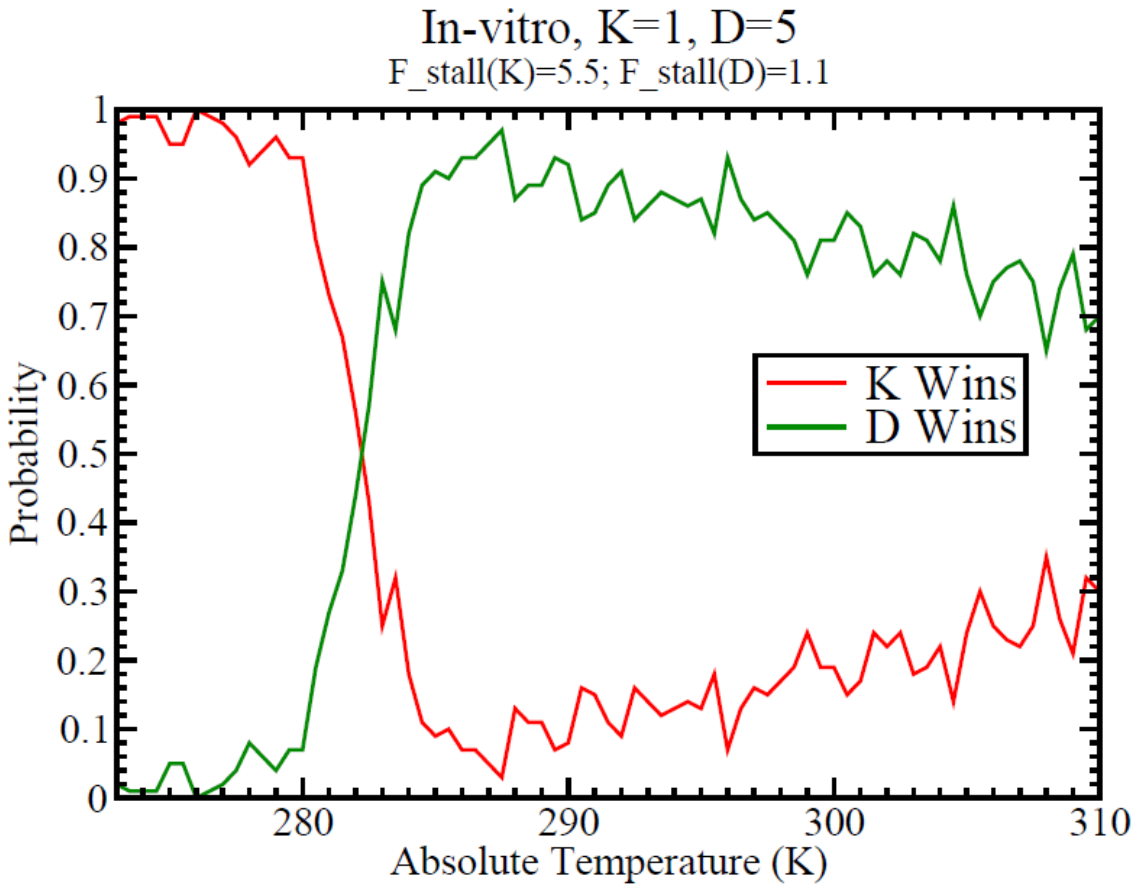

Figure 5.11 *In vitro* simulation of bead movement along MT. Red line shows the probability of bead moving to MT plus end, indicating kinesin wins; Green line shows the probability of bead moving to MT minus end, indicating dynein wins.

across the full temperature range. At temperatures below 280 K (~7 °C), kinesin almost always wins the tug-of-war and moves the bead toward the plus end of MT; above 284 K (~11 °C), dynein mostly wins the tug-of-war. The crossover point is around 282 K (~9 °C).

So how to interpret these results? The Arrhenius break for dynein is around 288 K (~15 °C). Above this temperature, dynein has a higher velocity than kinesin, and this trend follows up to physiological temperature 37 °C, as indicated from the measured activation energy. Since there are many more dyneins than kinesin, the minus end motion wins on average. At temperatures below the Arrhenius break, dynein's velocity drops much quicker than kinesin's. At low temperatures, kinesin still moves relatively fast while dynein almost stops; thus even though there is only one kinesin, it would win the tug-of-war because it is the only motor that still moves.

My results suggest that temperature has significant effects on bidirectional transport. The crucial qualitative result is that the overall direction of bidirectional transport can be reversed by increasing or decreasing temperature. The mechanism of how the motor ensembles are or can be tuned to switch direction would be interesting to study and helpful to understand the tug-of-war scenarios more completely.

5.8 References

(1). Kawaguchi, K.; Ishiwata, S. Temperature Dependence of Force, Velocity and Processivity of Single Kinesin Molecules. *Biochem. Biophys. Res. Commun.* **2000**, *272* (3), 895–899.

(2). Travers, F.; Barman, T.; Cryoenzymology: How to Practice Kinetic and Structural Studies. *Biochimie.* **1995**, *77* (12), 937–948.

(3). Richard, J.; McKenney, *et al.* Activation of Cytoplasmic Dynein Motility by Dynactin-Cargo Adapter Complexes. *Science* **2014**, *345* (6194), 337–341.

(4). Vale, R. D. Switches, Latches, and Amplifiers: Common Themes of G Proteins and

Molecular Motors. *J. Cell Biol.* **1996**, *135* (2), 291–302.

(5). Svoboda, K.; Block, S. M. Force and Velocity Measured for Single Kinesin Molecules. *Cell* **1994**, *77* (5), 773–784.

(6). Bohm, K. J.; Stracke, R.; Baum, M.; Zieren, M.; Unger, E. Effect of Temperature on Kinesin-Driven Microtubule Gliding and Kinesin Atpase Activity. *FEBS Lett.* **2000**, *466*, 59–62.

(7). Kull, F. J.; Sablin, E. P.; Lau, R.; Fletterick, R. J.; Vale, R. D. Crystal Structure of the Kinesin Motor Domain Reveals a Structural Similarity to Myosin. *Nature* **1996**, *380* (6574), 550–555.

(8). Toprak, E.; Yildiz, A.; Hoffman, M. T.; Rosenfeld, S. S.; Selvin, P. R. Why Kinesin is so Processive. *Proc. Natl. Acad. Sci. U S A.* **2009**, *106* (31), 12717–12722.

(9). Hancock, W. O. Bidirectional Cargo Transport: Moving Beyond Tug-of-War. *Nat. Rev. Mol. Cell Biol.* **2014**, *15* (9), 615–628.

(10). Soppina, V.; Rai, A.; Ramaiya, A.; Barak, P.; Mallik, R. Tug-of-war between Dissimilar Teams of Microtubule Motors Regulates Transport and Fission of Endosomes. *Proc. Natl. Acad. Sci. U S A.* **2009**, *106* (46), 19381–19386.

(11). Tucker, R.; Saha, A. K.; Katira, P.; Bachand, M.; Bachand, G. D.; Hess, H. Temperature Compensation for Hybrid Devices: Kinesin's Km is Temperature Independent. *Small* **2009**, *5* (11), 1279–1282.

CHAPTER 6

CONCLUSION

We constructed a microscope setup, with two optical trappings capabilities, conventional trapping, and holographic trapping. This setup is capable of precisely manipulating micron-sized beads, as well as tracking their positions with high spatial and temporal resolution. This allows us to study the molecular motors properties at a single-molecule level and allows us to build complexity in a controlled way.

My work was the first in the Vershinin lab to look at the chemical regulation of motors. I looked at the kinesin motors inhibition by marine natural compound adociasulfates and confirmed that adociasulfates inhibit kinesins activity by competing with microtubules and thus prevent kinesins from binding to microtubules. By comparing the inhibition effect of kinesins by two structurally similar adociasulfates, I concluded that substitution of the sulfate residue on adociasulfates to other negatively charged residue does not dramatically change the inhibition effect, which provided a roadmap for how adociasulfates cell permeability can be improved. I did not detect any aggregates of adociasulfates, which was reported earlier by others, and proved that aggregates are not required for inhibition.

By comparing the adociasulfates inhibition on different kinesin family motors, I found that adociasulfates preferentially inhibit conventional kinesins over mitotic kinesins. These findings greatly increased the value of adociasulfates as a pro-drug candidate and lead to further work in our lab regarding regulation of kinesin binding to microtubules.

I have also started measurements of biophysical motor regulation (via temperature). I used a few noncontact methods to calibrate the solution temperature in a small volume, using the properties of thermal shifts of quantum dots fluorescence, the changes of beads diffusion coefficient with temperature, and the substance freezing/melting point measurements.

I studied the temperature dependent properties of kinesin and dynein motors. I found that while kinesins' velocities decrease according to the Arrhenius relationship at the full temperature range, dyneins' velocities show piece-wise Arrhenius decay with a break at ~15 °C. Below this temperature, dyneins' velocity decreases much faster than kinesins'. Kinesin and dynein forces do not measurably change with temperature. Simulations based on these results showed that the overall direction of bidirectional transport can be reversed by increasing or decreasing temperature. Thus temperatures have significant effects on bidirectional transport and may be useful for studying the mechanism of tug-of-war between kinesin and dynein motors.